ELSEVIER

Coordination Chemistry Reviews
219–221 (2001) 17–52

COORDINATION CHEMISTRY REVIEWS

www.elsevier.com/locate/ccr

Chemistry, properties and applications of the assembling 1,8-diisocyano-*p*-menthane, 2,5-dimethyl-2′,5′-diisocyanohexane and 1,3-diisocyanopropane ligands and their coordination polynuclear complexes

Pierre D. Harvey *

Département de Chimie, Université de Sherbrooke, Sherbrooke, Canada, J1K 2R1

Received 27 June 2000; accepted 3 October 2000

This paper is dedicated to Professor Barry A.P. Lever on the occasion of his 65th birthday

Contents

* Tel.: +1-819-8217092; fax: +1-819-8218017.

0010-8545/01/$ - see front matter
PII: S0010-8545(00)00415-X

Abstract

This review article presents an overview of the coordination chemistry of the three title bridging ligands, along with some selected structural, vibrational and electronic spectroscopic, photo- and electrochemical, and catalytic properties. These ligands can bridge metal atoms to form bi-, tri, and tetranuclear complexes and polymers. Solid state properties for the polymeric materials such as glass transitions, intrachain exciton phenomena, semi- and photoconductivity, as well as the design of photovoltaic cells are briefly described.

Keywords: Isocyanides; Bridging ligands; Polynuclear complexes; Polymeric materials

1. Introduction

The first preparations and investigations of the title compounds (Fig. 1) go back to the early work of Gray et al. in the mid 1970s [1–4], and was motivated by the investigations on oligomerization of the square planar $Rh(CNR)_4^+$ species. It was quickly recognized that the M_2 interactions were responsible for such phenomena, but the nature of the oligomers was concentration dependent, and more than one oligomer could be present in solutions at the same time. The use of the assembling

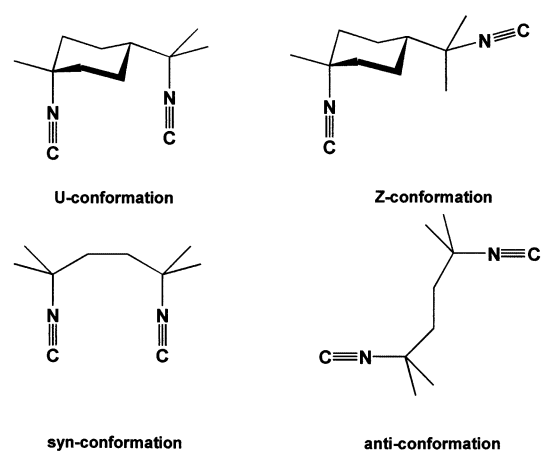

Fig. 1. Various conformations for the tmb and dmb ligands.

title ligands then allowed the preparation of better defined M_2 systems, with M_2 distances that could also be directed depending on the bite distance of the selected ligand.

The major early contribution for potential applications came from Professor Gray's research on solar energy conversion via the use of 'windmill' Rh(I) complexes of the type $Rh_2(diiso)_4^{2+}$ with diiso being the bridging ligands b, tmb, and dmb. Indeed, the stoichiometric photo-induced H_2 evolution was reported [1–4]. Following these years was a relatively quiet period, during which Mann et al. reported several papers on these interesting systems among which one can find preparation of exotic versions of these dmb complexes, including the mixed ligand $Rh_2(dppm)_2(dmb)_2^{2+}$ and heteronuclear trimetallic species [5–7]. In 1993, our group reported the first organometallic polymer of the dmb ligand [8], and a series of works in this area led to the discovery of new semi-conducting and photo-conducting materials [9].

We now wish to report an overview on these ligands and their coordination complexes and the many special features and applications that such compounds provided over a short period of time. Phenomena such as encapsulation of halogens and metals, CO_2 and C–H bond activation, intra molecular excitons, electrocatalysis, synthesis of tetranuclear linear clusters and catenates, polymer isomerization, semi- and photoconductivity will be presented and discussed. To our knowledge this is the only existing review which deals with these ligands.

2. Ligand syntheses

Although several methods exist for the preparation of isocyanide species [10] the carbene method using chloroform, sodium hydroxide in refluxing dichloromethane is the most favored method [11], where the one step recipe gives yields ranging from 30 to 50% with the commercially available 1,3-diaminopropane, 2,5-dimethyl-2′,5,-diaminohexane, and 1,8-diamino-*p*-menthane starting materials. This synthesis appears to be more convenient than the two-step procedure with the formamide species, followed by the dehydration reaction using phosgene or diphosgene. The purification of dmb and tmb can proceed via recrystallization in ethanol. dmb and tmb are both very crystalline white materials. b is separated and purified by distillation. A strong ν(C≡N) peak between 2020 and 2040 cm^{-1} in the IR spectra characterizes the ligands. The ^{1}H-NMR spectrum is simple, and consists of a multiplet at $\sim$1.4 ppm. b is separated and purified by distillation.

3. Binuclear species

3.1. The d^{10}–d^{10} M_2(diiso) complexes

The series of complexes is dominated by the Au(I) metal, and its diiso complexes have the general formula $Au_2(diiso)(X)_2$ where diiso = tmb and dmb, and X = Cl,

CN and C≡Ph. The ligands adapt primarily to the anti-conformations (tmb) and *Z*-conformations (dmb), precluding any intramolecular M…M interactions. The only exception is the $Au_2(dmb)(CN)_2$ complex where a U-conformation is observed according to X-ray data [12]. The cyano derivatives are prepared in methanol using the $AuCl_4^-$ precursor according to:

$$2AuCl_4^- + \text{diiso(excess)} \rightarrow Au_2(\text{diiso})(CN)_2 + \text{other products} \quad (1)$$

Che et al. tentatively explained this result via an out-of-sphere electron transfer reaction involving both the coordinated diiso ligand and the methanol in the process [13]. In contrast, a second product was reported by Harvey et al. under the same conditions, where the crystallographically characterized $Au_2(tmb)Cl_2$ was also formally identified [14]. The above mechanism may be somewhat more complex than anticipated. The reactivity of $PtCl_4^{2-}$ with CN-*t*-Bu in acetone illustrates this complexity, as the two observed products are the expected *cis*-$Pt(CN\text{-}t\text{-}Bu)_2Cl_2$ and the bridged binuclear $Pt(CN\text{-}t\text{-}Bu)_2Cl(\mu\text{-}CN)Pt(CN\text{-}t\text{-}Bu)Cl_2$ [15]. In these cases, the Pt(II) atom does not change oxidation state. In the solid state the $Au_2(dmb)(CN)_2$ compound exhibits a rather short Au…Au distance of ~ 3.54 Å in comparison with the sum of the van der Waals radii (3.60 Å) as discussed in this paper. Very clear deviations of the CAuC angles are reported, but the most striking results come from the observation of a strong $\nu(Au_2)$ scattering at 36 cm^{-1} [16]. This assignment was confirmed from the measurements of polarized Raman spectra of a single crystal. In addition, a graph of the d(Au…Au) data versus ln *F* (Au…Au) ($F = 0.075$ mdyn $Å^{-1}$; diatomic model) follows the linear correlation closely, despite the fact that the distance between the two Au atoms of 3.54 Å is at the limit of the sum of the van der Waals radii. On the other hand the $Au_2(tmb)(Cl)_2$ exhibits a polymeric structure in the solid state via weak intermolecular Au…Au interactions (~ 3.30 Å). The tmb bridging ligand adopts an anti-configuration. In this case the Raman spectra exhibit a strong scattering at ~ 50 cm^{-1} attributable to $\nu(Au_2)$ [14].

The other mono-diisocyanide dinuclear complex $Au_2(dmb)(C{\equiv}CPh)_2$, [17] is also a luminescing complex. Due to the *Z*-conformation, no M…M intramolecular interaction is possible, but intermolecular Au…Au chains are obvious in the solid state. These distances are 3.329(2), 3.565(2) and 3.485(3) Å for the related complexes $PhC{\equiv}C\text{–}Au\text{–}C{\equiv}N\text{–}C_6H_3(CH_3)_2$, $Au_2(tmb)(C{\equiv}CPh)_2$, respectively [17]. Evidence of Au…Au interactions in the solid state are also found in UV–vis spectroscopy where the strong absorption associated with the Au_2 metal-centered electronic transition $d\sigma^* \rightarrow p\sigma$ [17] follows a qualitative relation with the metal–metal separations. For instance λ_{max} absorptions are 210, ~ 230 and 292 nm, for the $M(CN\text{-}t\text{-}Bu)_4^+$ (M = Cu, Ag; i.e. no M_2 interactions) [18], $Au_2(dmb)(CN)_2$ [12], and $Au_2(tmb)Cl_2$ complexes [14], respectively, where the M…M distances are $\ll 5$ Å, ~ 3.6 and ~ 3.3 Å, respectively.

The photophysical data for these species are presented in Table 1. There is a marked difference between the two series of complexes. On one side, the phenylacetylenyl derivatives exhibit vibrationally structured absorption and emission bands which were analyzed as MLCT bands from the d^{10} Au(I) metal to the

Table 1
Spectroscopic and photophysical data for Au(CNR) species [a]

Complexes	λ_{abs} (nm)	λ_{emi} (nm)	τ_e (μs)	Assignment	Reference
(PhC≡C)Au(CNR) [b]	274, 288	419 (CH_2Cl_2)	7.65	MLCT	[17]
Au_2(tmb)(C≡CPh)$_2$	274, 288	420 (CH_2Cl_2)	5.40	MLCT	[17]
Au_2(dmb)(C≡CPh)$_2$	277, 288	420 (CH_2Cl_2)	2.50	MLCT	[17]
Au_2(tmb)Cl_2	292	417 (KBr)	0.70	dσ* → pσ	[14]
Au_2(tmb)$(CN)_2$	290				[13]
Au_2(dmb)$(CN)_2$	230	456 (solid)	0.59	dσ* → pσ	[12]
		458 (CH_2Cl_2)	0.13	dσ* → pσ	

[a] Room temperature data.
[b] R = $CNC_6H_3(Me)_2$.

phenylacetylenyl π* system. The long emission lifetimes (τ_e, which range from 2.5 to 7.7 μs), and the large energy gap between the absorption and emission (Stokes shift = 11000 cm^{-1}) indicate that the luminescence is a phosphorescence. On the other hand, the Au_2(tmb)Cl_2 and Au_2(dmb)$(CN)_2$ dimers exhibit structureless emissions which were assigned to a dσ*–pσ electronic transition. Their emission were also interpreted in terms of phosphorescence, except that τ_e ranges from 130 to 700 ns, even in the solid state. This observation can be rationalized as a greater non-radiative rate constant associated with lower vibrational frequencies involved in the excited state deactivation processes. Intuitively, the dσ*–pσ excited states associated with weak Au…Au interactions which involve $\nu(Au_2)$ of about 30–50 cm^{-1}, in comparison with the more rigid Au–C≡C–Ph fragment in which the MLCT process takes place, could be at the origin of this difference. More importantly, in this series the alkyl isocyanide fragment does not appear to be involved in the photophysical processes.

3.2. The d^{10}–d^{10} M_2(diiso)$_2$ complexes

The second family of dinuclear compounds are the $M_2(dmb)_2X_2$ species (M = Cu, Ag; X = Cl^-, Br^-, I^-, NO_3^-, $CH_3CO_2^-$ and ClO_4^-) [18–21]. These complexes are obtained via the direct reaction between the corresponding Ag salt, and the ligand, with the appropriate stoichiometric amount. The structure consists of a cyclic $M_2(dmb)_2^{2+}$ fragment, doubly bridged by halides or an oxygen atom of the oxo ligand (Fig. 2). The Ag atoms exhibit a highly distorted tetrahedral geometry, associated with the sharp XAgX angles, and the relatively long bite distance of the dmb ligand. In addition, there is a remarkable trend between the formal charge of the bridging atom and the Ag…Ag separations, where the weaker the charge (−1, −0.5, −0.33), the longer the distance is (Table 2). This behavior illustrates the ionic contribution to the Ag–X and Ag–O bonds in these cases. For the $Cu_2(dmb)_2I_2$ complex, the shorter Cu…Cu distance is consistent with the smaller cationic radii for Cu^+ (0.91 versus 1.08 Å for Ag^+ [22]). Evidence of Ag…Ag interactions were clearly obtained from both Raman and UV–vis spectroscopies

[19,20]. The $\nu(Ag_2)$ data are 42, 42, and 33 cm^{-1} [20], and the $\lambda(d\sigma^*-p\sigma)$ maxima are 232, 241, and 242 nm [19] for X = Cl, Br, I, respectively. These species are also found to be luminescent, but only in glassy matrices at low temperatures. The emission bands are recorded in the 400–700 nm window where the λ_e range from 440 to 470 nm, and τ_e are found to be 24–29 μs in solutions (ethanol, 77 K) and 33–80 μs in NaCl pellets at 77 K, exhibiting an obvious trend Cl > Br > I associated with the greater spin-orbit couplings of the heavier halides [19]. These low energy absorptions and emissions were assigned to metal/halide-to-ligand

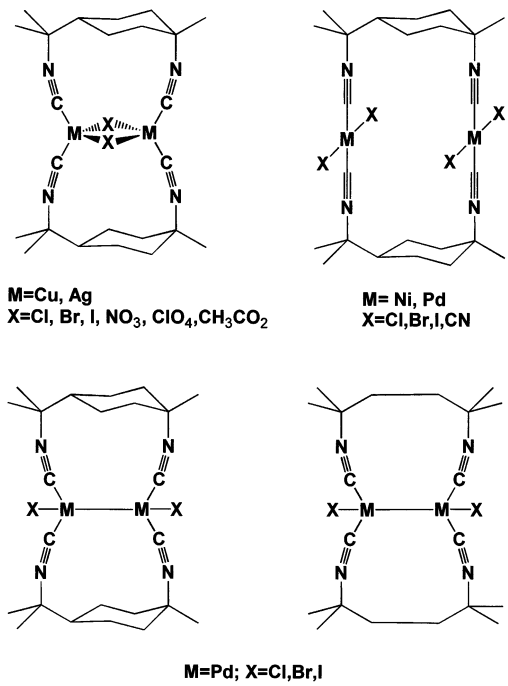

Fig. 2. Molecular structures for the d^{10}–d^{10} $M_2(dmb)_2X_2$ (Top left), d^8–d^8 $M_2(dmb)_2X_4$ (Top right), and the d^9–d^9 $M_2(diiso)_2X_2$ complexes (Bottom; diiso = dmb and tmb).

Table 2
Structural and spectroscopic data for $M_2(dmb)_2X_2$ complexes [a]

Complexes	d(M…M) (Å)	$\nu(M_2)$ (cm^{-1})	$\lambda_{max}(d\sigma \rightarrow d\sigma^*)$ (nm)	Reference
$Ag_2(dmb)_2Cl_2$	3.451(2)	42	232	[19,20]
$Ag_2(dmb)_2Br_2$	3.345(1)	42	241	[19,20]
$Ag_2(dmb)_2I_2$	3.378(2)	33	242	[19,20]
$Cu_2(dmb)_2I_2$	3.199(10)			[18]
$Ag_2(dmb)_2(NO_3)_2$	3.9075(14)			[21]
$Ag_2(dmb)_2(O_2CMe)_2$	3.6832(7)			[21]

[a] Room temperature data. The UV–vis data; solvent = ethanol at 77 K.

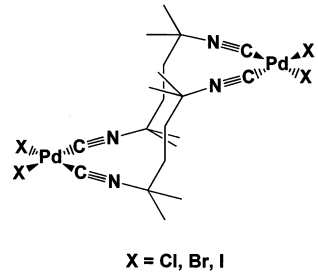

Fig. 3. Side view of the d^8–d^8 $Pd_2(tmb)_2X_4$ complexes.

Table 3
List of known $M_2(dmb)_2X_4$ complexes

Complexes	d(M…M) (Å)	Reference
$Ni_2(dmb)_2(CN)_4$	4.33	[25]
$Pd_2(dmb)_2(Cl)_4$	4.399(2)	[24]
$Pd_2(dmb)_2Cl_2Br_2$ [a]	4.466(2)	[24]
$Pd_2(dmb)_2Br_4$		[24]
$Pd_2(dmb)_2I_4$	4.582(1)	[23]
$Pt_2(dmb)_2Cl_4$		[85]

[a] The Br atoms are the weakly interacting bridging ligands.

charge transfers (M/XLCT) on the basis of EHMO computations and the measurements of polarized emission spectra.

3.3. The d^8–d^8 $M_2(diiso)_2$ complexes

These complexes are the $M_2(dmb)_2X_4$ (M = Ni, Pd, Pt; X = Cl, Br, I, CN) and $Pd_2(tmb)_2X_4$ species. The structure of the former family consists of square planar M(II) fragments placed face-to-face via two dmb bridging ligands (Fig. 2). These complexes are obtained from the direct reaction between the commercially available $PdCl_2$ or the common $PdCl_2(NCPh)_2$ starting materials, and the diisocyanide ligand in slight excess. In these cases the local coordination is *trans*-, and contrasts with the tmb analogues where the PdX_2 residues adopt a *cis*-configuration (Fig. 3) [23–25]. For the dmb species, the face-to-face geometry allows the metals to be placed about 4.3 to 4.6 Å from each other (Table 3). However the planes rotate along the CMC axes to favor some closer Pd…X contacts. This is well illustrated by the short non-bonding Pd…Cl distance of 3.473(3) Å in the $Pd_2(dmb)_2Cl_4$ complex, and by the significant non-bridging (2.475(3)) and bridging (2.385(3) Å) Pd–Cl bond lengths [24]. The variation of the non-bonding Pd…X distances (X = Cl, 3.473; X = Br, 3.662; X = I, 3.852 Å) as expected, follows the atomic size of the halides. As a consequence, the M…M distances follow the same trend ($d \sim 4.3$, 4.4, 4.5, 4.6 for X = CN, Cl, Br, I, respectively). In the absence of such

interactions one can easily anticipate an insensitivity of the M…M distance with X. In contrast with the Ag(I) and Au(I) complexes presented above, no luminescence has been reported in these cases, either for solutions or solid samples between 77 and 293 K.

3.4. The d^9–d^9 $M_2(diiso)_2$ complexes

These complexes include the M_2-bonded d^9–d^9 $Pd_2(diiso)_2X_2$ dimers (diiso = dmb and tmb; X = Cl, Br). Their preparations are analogous to that of the $Pd_2(dppm)_2X_2$ complexes, and are as follows:

$$Pd_2(diiso)_2X_4 + Pd_2(dba)_3 + 2\ diiso \rightarrow 2\ Pd_2(diiso)_2X_2 + 3\ dba \quad (2)$$

The structure consists of a Pd–Pd single bond supported by two diiso bridging ligands. The two halide atoms axially coordinate the vacant sites on the Pd–Pd bond. No X-ray structure has been obtained so far for these electron-rich species, but evidence for the M–M bond has clearly been established using resonance Raman spectroscopy and UV–vis measurements of the dσ–dσ* band as a function of temperature [26]. The M_2 distance in these cases has been estimated to be about 2.72 ± 0.05 Å [26] using the vibrational data ($\nu(Pd_2)$ and $\nu(PdX)$) and an empirical equation relating specifically the Pd_2 force constant with the bond length [20,27]. Although this distance appears somewhat long in comparison with other d^9–d^9 'Pd–CNR' species ($2.53 < d(Pd2) < 2.56$ Å) [26]. Considering the uncertainty it also compares reasonably to that reported for $Pd_2(CNC_6H_3(Me)_2)_4(Py)_2^{2+}$ (2.66 Å) [28]. The most striking evidence is the clear relationship between the λ(dσ–dσ*) band position with $d(Pd_2)$ (see Table 4), where the longest $d(Pd_2)$ data imply shorter dσ/dσ* energy gaps, as anticipated. Surprisingly, this long distance has not been confirmed theoretically using DFT computations (density functional theory) [29]. The computed Pd_2 bond length in $Pd_2(tmb)_2Cl_2$ was unexpectedly shorter (2.588 Å)

Table 4
Spectroscopic data for M_2-bonded CNR complexes [a]

Complexes	$d(M_2)$ (Å)	$\nu(M_2)$ (cm^{-1})	λ_{max}(dσ → dσ*) (nm)	λ_{emi} (nm)	τ_e (μs)
$Pd_2(dmb)_2Cl_2$	2.72	174	448	625	0.071
$Pd_2(dmb)_2Br_2$	2.72	131	446	650	0.177
$Pd_2(tmb)_2Cl_2$	2.72	172	426	625	0.081
$Pd_2(tmb)_2Br_2$	2.72	129	420	650	0.125
$Pd_2(CNR)_4(Py)_2^{2+}$ [b]	2.662		377		
$Pd_2(CNR)_4Cl_2$ [c]	2.562		324		
$Pd_2(CN\text{-}t\text{-}Bu)_4Cl_2$	2.532		307		
$Pd_2(CNMe)_6^{2+}$	2.531	160	302		

[a] The data for the dmb and tmb species are at 77 K in ethanol. The Raman data are from resonance Raman experiments. The 2.72 Å data are spectroscopically evaluated (± 0.05 Å). All data are from Ref. [26] and the references therein.

[b] $R = C_6H_3(Me)_2$.

[c] $R = C_6H_2(Me)(t\text{-}Bu)_2$.

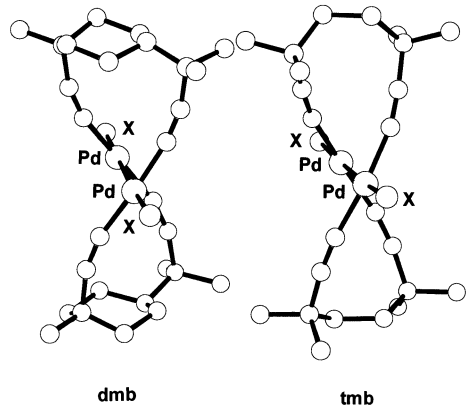

Fig. 4. View along the Pd_2 bonds in the $Pd_2(diiso)_2X_2$ complexes (diiso = dmb, tmb; X = Cl, Br).

[29], but the optimized structure kept an unusual PdPdC angle of 90° despite the obvious ring stress. The comparison between the calculated (2.523 Å) and experimental (2.532 Å) Pd_2 bond lengths in the unsupported $Pd_2(CNR)_4Cl_2$ species [29], is good, and the increase (by 0.01 Å) goes in the right direction when considering the computational data for the tmb bridged species. As the skeleton of the $Pd_2(diiso)_2X_2$ complexes is obviously not planar, computer modelings (PC-model) readily predict a significantly twisted structure (Fig. 4). These ligands appear very flexible allowing Pd_2 bonding to occur. The computed dihedral angles are 62 and 72° for the tmb and dmb derivatives, respectively.

In contrast with the Ni(II) and Pd(II) species of the previous section, the Pd(I) complexes are weakly luminescent at 77 K in glassy matrices. The emission bands appear in the 600–700 nm range, and the τ_e data indicate that the excited lifetimes are very short ($71 < \tau_e < 177$ ns). These emissions have been assigned to a phosphorescence due to the large Stoke shifts, and arise from a triplet $d\sigma$–$d\sigma^*$ state, based on EHMO computations which indicated that no other lower energy state existed, at least according to this model. Room temperature flash photolysis measurements do indeed confirm the very short excited state lifetime ($\tau < 20$ ps), perhaps corroborating the absence of luminescence at this temperature [26]. Despite these short lifetimes, photochemical oxidation of these species by chlorocarbons readily produces the non-Pd_2 bonded complexes $Pd_2(diiso)_2X_2X'_2$ (X = Cl, Br; X′Cl)[24]. These short excited state lifetimes have been interpreted in terms of efficient homolytical Pd–Pd bond scission in the triplet $d\sigma$–$d\sigma^*$ state.

Cyclic voltammetry measurements on the $Pd_2(dmb)_2X_2$ complexes (X = Cl, Br, I) indicate the presence of irreversible one-electron waves at $+0.78$, $+0.64$, and $+0.38$ V versus SCE, respectively [26]. This relative ease with which the $Pd_2(dmb)_2X_2$ complexes are oxidized may explain the dismutation reaction described below. On the other hand, no reduction wave was found for potentials less negative than -1.5 V versus SCE. For comparison purposes, the $Pd_2(dppm)_2X_2$

species exhibit irreversible two-electron waves at -1.26, -1.23 V and versus SCE [30].

$Pd_2(dmb)_2Cl_2$ reacts with PPh_2Me in slight excess to unexpectedly form the colorless binuclear $[Pd_2(dmb)_2(PPh_2Me)_4(\mu\text{-}Cl)](Cl)_3$, and an uncharacterized red and air-sensitive compound [31]. This reaction appears as a dismutation of the type $2Pd(I) = Pd(II) + Pd(0)$. On the basis of the close resemblance of the UV–vis spectra, the true nature of this red compound could be a polynuclear complex somewhat related to the known low-valent linear cluster $Pd_4(dmb)_4(PPh_3)_2^{2+}$ discussed below. The X-ray results on the white crystal reveal again a face-to-face structure where the PdC_2P_2 centers adopt the common *trans*-geometry [31]. The main feature is the encapsulation of a Cl anion retained inside the cavity by the four Me groups and two dmb ligands (Fig. 5). The Pd…Pd distance is 5.5534(6) Å, placing the Pd…Cl interactions well within the sum of the van der Waals radii (~ 3.5 Å). As a consequence, the CPdC angles deviate somewhat from linear (175.0(1.1)°). The encapsulation of halide ions within the $M_2(dmb)_2$ skeleton was first observed by Gladfelter and Gray [32], using UV–vis spectrometric methods, and molar conductivity measurements, for $Ni_2(dmb)_4(\mu\text{-}X)^{3+}$ complexes (X = Cl, Br). These species belong to the d^8–d^8 $M_2(diiso)_4$ series discussed below.

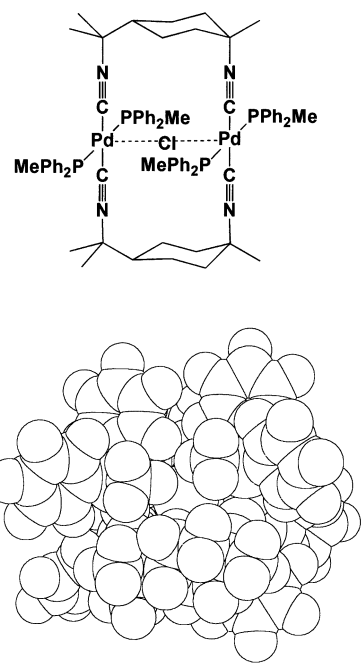

Fig. 5. CPK model of the $Pd_2(dmb)_2(PPh_2Me)_4(\mu\text{-}Cl)^{3+}$ complex. The Cl^- ion is somewhat visible in the middle of the CPK drawing.

Table 5
Selected structural and spectroscopic data for d^8–d^8 $M(CNR)_4^+$

Complexes	$d(M_2)$ (Å)	$\nu(M_2)$ (cm^{-1})	$\lambda_{max}(d\sigma \rightarrow d\sigma^*)$ (nm)	Reference
$Rh_2(CN\text{-}p\text{-}tol)_8^{2+}$			562	[36]
$Rh_2(CNPh)_8^{2+}$	3.193	60		[35,37]
$Rh_2(b)_4^{2+}$	3.243	79	553	[36–38]
$Rh_2(4\text{-}b)_4^{2+}$ [a]			526	[39]
$Rh_2(tmb)_4^{2+}$	3.262	55	514	[38,39,42]
$[Rh_2(dmb)_4](PF_6)_2$	4.479		420	[40]
$[Rh_2(dmb)_4](TFBP)_2$ [b]	4.246		428	[41]
$[Rh_2(dmb)_4](BPh_4)_2$	3.861	28	437	[41,43]
$[Ir_2(tmb)_4](PF_6)_2$	3.119	53		[42,44]
$[Ir_2(tmb)_4](BPh_4)_2$	3.16, 3.24		625	[44,45]
$[Ir_2(dmb)_4](PF_6)_2$	4.415		468	[41]
$[Ir_2(dmb)_4](TFBP)_2$	3.944		534	[41]
$[Ir_2(dmb)_4](BPh_4)_2$	3.601		580	[41]

[a] 4-b = 1,4-diisocyanobutane.
[b] TFPB = tetra-*p*-fluorophenylborate.

3.5. The d^8–d^8 $M_2(diiso)_4$ complexes

The early development of the d^8–d^8 diisocyanide chemistry finds its origin in the face-to-face oligomerization of the square planar $Rh(CNR)_4^+$ species [33,34]. Species such as $[Rh(CNR)_4]_n^{n+}$ where $n = 1,2,3$, and R = Ph, *t*-Bu, *i*-Pr, Cy, and vinyl have been demonstrated to exist in solutions from the non-linearity of the Beer–Lambert law in the UV–vis spectra [33,34], and the dimeric complex $[Rh(CNPh)_4]_2(BF_4)_2$ has been characterized from crystallography [33]. In this case the non-bonding Rh_2 distance is 3.193(1) Å. A strong band which is assigned to $1b_2$(anti-bonding combination of the d_{z2} orbitals) to $2a_1$ (bonding combination of the π^* (CNR) orbitals), eventually renamed $d\sigma^*$–$p\sigma$, is located in the 490–570 nm range for the dimeric species, and found between 610 and 730 nm in the trimeric ones [33]. Gray et al., then reported the preparation of the first diisocyano-alkane complex in 1976 [35], formulated as $Rh_2(b)_4^{2+}$. Soon after this paper, his group reported the first results on the excited reactivity in relation with the dinuclear redox center which may lead to bond breaking and bond formation [4] in view of solar energy conversion. Indeed $Rh_2(b)_4^{2+}$ reacts with HCl to generate the hydride species $[Rh_2(b)_4(H)]Cl$. Subsequent irradiation of the solution at 546 mn leads to the clean conversion of the species into the d^7–d^7 $[Rh_2(b)_4Cl_2]^{2+}$ complex and H_2. Since this early work and exhaustive series of studies on the mechanistic aspects of this reaction and on the spectroscopic properties of these species followed. These results are presented summarily here.

Table 5 lists selected structural and spectroscopic data for Rh(I) and Ir(I) binuclear complexes (Fig. 6) [35–45]. These compounds exhibit a so-called windmill structure where the M…M separation is first predictable a function of the assembling ligand (b < tmb < dmb), the metal (Rh > Ir; i.e. weaker M…M interactions),

and the counter anion. The shorter the distance is, the greater the dihedral twist angle is. This feature was striking in the $M_2(dmb)_2^{2+}$ species (M = Rh, Ir) [41,42]. Evidence for M…M interactions in the ground state was clearly provided from resonance Raman spectroscopy where $\nu(M_2)$ are found below 100 cm^{-1} [41]. There is a quasi-relationship between $\nu(M_2)$ and $d(M_2)$ as expected, despite the fact that the M_2^* separations may be different in solutions and in the solid state.

As stated, the $d\sigma^* \rightarrow p\sigma$ electronic band generated from these weak M_2 interactions are located between 420 and 625 nm. Again a relationship between the M_2 distance and λ_{max} has been demonstrated for both the solution and solid state data. A special feature in the dmb chemistry is that the $M_2(dmb)_4^{2+}$ for both the Rh and Ir derivatives, exhibit a very shallow potential energy surface [41,43].

Excitation in the $d\sigma^*-p\sigma$ induces a strong M_2-distance shortening in both singlet and triplet excited states. For $Rh_2(b)_4^{2+}$, polarized absorption spectra measured on a single crystal (as a BPh_4^- salt) at 5 K exhibits a strong vibrationally resolved progression averaging 150 cm^{-1} [46]. This vibrational mode has been assigned to $\nu(Rh_2)$ in the $^1(d\sigma^*-p\sigma)$ excited state associated with the formation of a formal Rh–Rh single bond. In addition, time-resolved resonance Raman spectroscopy established that $\nu(Rh_2) = 144$ cm^{-1} in the $^3(d\sigma^*-p\sigma)$ excited state [37]. Similarly, using time-resolved IR spectroscopy, the ν(RhC) and ν(C≡N) data were measured in both the ground and excited states (Table 6) [47]. Rh–C bond shortening (-0.022 Å) and C≡N bond lengthening ($+0.002$ Å) are observed in the $^3(d\sigma^*-p\sigma)$ excited state, consistent with a model that involves some Rh–CNR(π^*) character (i.e. MLCT). In addition, $\nu(Rh_2)$ in the $^3(d\sigma^*-p\sigma)$ excited state for $M_2(tmb)_4^{2+}$ is

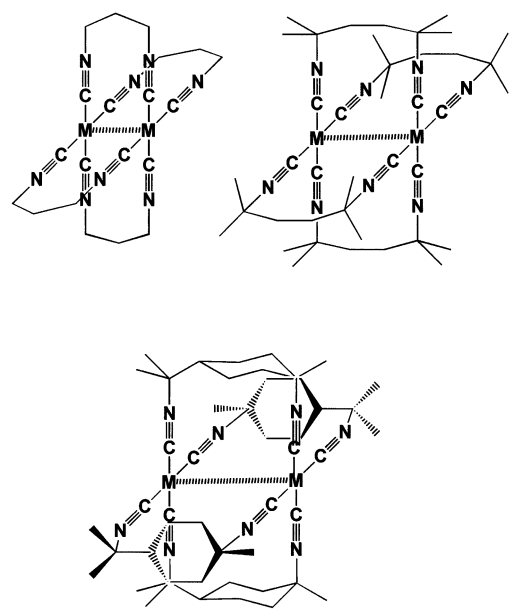

Fig. 6. Windmill structures of the d^8-d^8 $M_2(diiso)_4^{2+}$ complexes (M = Rh, Ir; diiso = b, tmb, dmb).

Table 6
Selected structural and spectroscopic data for $Rh_2(b)_4^{2+}$ [47]

Mode (cm^{-1})	$^1(d\sigma^* \rightarrow p\sigma)$	$d(Rh_2)$ (Å)	$^3(d\sigma \rightarrow p\sigma)$	$d(Rh_2)^*$ (Å)	Δ (Å)
$\nu(Rh_2)$	79	3.175	144	2.965	−0.210
$\nu(RhC)$	467	2.253	484	2.231	−0.022
$\nu(C\equiv N)$	2193	1.132	2177	1.134	+0.002

also in the same order of magnitude ($\nu(Rh_2) = 151$ [37] and $\nu(Ir_2) = 132\ cm^{-1}$ [44]), leading to the same conclusion about the change in bond order in the excited state.

These species exhibit rich photophysical properties at room temperature and in fluid solutions [36,39,43,44,48–53] and fluorescence and phosphorescence spectra have been reported for most of the Rh and Ir binuclear species (Table 5). The fluorescence is characterized by a structureless band located between 500 and 700 nm, and τ_e ranging from 0.2 to 1.1 ns with modest fluroescence quantum yields ($0.0025 < \phi < 0.077$). The more red-shifted phosphorescence ($660 < \lambda_{max} < 830$ nm) exhibits more variable τ_e and ϕ_e data. It appears that τ_e and ϕ_ε vary as b > tmb > dmb, which may indicate the effect of ligand flexibility on the excited state deactivation rate constants. However the phosphorescence τ_e data are found to be greatly temperature dependent [49] ($\tau_P = 25$ ns versus 20 μs for $Rh_2(tmb)_4^{2+}$ and $\tau_P = 9$ and 16 μs for $Rh_2(b)_4^{2+}$ at 294 and 77 K, respectively).

$Ir_2(tmb)_4^{2+}$ exhibits photo-induced H-abstraction reactivity [42,44,54]. This dimer in the presence of hydrogen donors such as 9,10-dihydroanthracene or 1,3-cyclohexadiene photo-generates anthracene, and benzene, respectively, along with the d^7–d^7 dihydride complex $Ir_2(tmb)_4H_2^{2+}$. Measurements of Stern–Volmer quenching rate constants demonstrate a relationship between the rate and the C–H bond dissociation energy, suggesting an homolytic C–H bond activation. Orientation of the C–H…M moieties and steric hindrance appeared important in the reactivity. Similarly these d^8–d^8 species photoreact with halocarbons to produce the d^7–d^7 $M_2(diiso)_4X_2^{2+}$ complexes (M = Rh, Ir; diiso = b, tmb, dmb; X = Cl, Br, I), along with the organic products, also via atom-abstraction reactivity in the excited states.

The electrochemical properties of the $M_2(dmb)_4^{2+}$ complexes (M = Rh, Ir; counter anion = PF_6^-, ClO_4^-, BPh_4^-) have been reported by Mann et al. [55–57]. The $Rh_2(dmb)_4^{2+}$ species can undergo a 2-electron oxidation at +0.46 V versus Ag/AgCl (counter anion = ClO_4^-) [57]. The oxidized species $Rh_2(dmb)_4^{4+}$ has some tendency to bind the Cl^- anions, presumably towards the reversible formation of the $Rh_2(dmb)_4Cl^{3+}$ and $Rh_2(dmb)_4Cl^{2+}$ complexes. The reduction peak of the 4^+ species greatly shift with the solvent and can be found at −0.28 V in acetonitrile–Bu_4NPE_6, and at +0.32 V in CH_2Cl_2.

Smith and Gray also reported the electro-catalytic oxidation of 1,4-cyclohexadiene into benzene in the presence of $Rh_2(dmb)_4^{4+}$ [54]. The process is accompanied by an enhanced anodic current with the loss of the cathodic wave. The overall reaction is described as C_6H_8=$C_6H_6 + 2e^- + 2H^+$ ($E° = 0.4$ V versus NHE). In the presence of CH_2Cl_2 as a solvent, the catalyst is slowly lost to form the inert

$Rh_2(tmb)_4Cl_2^{2+}$. The authors proposed a pathway to explain this reaction and oxidation of $Rh_2(tmb)_4^{2+}$ into the reactive d^8–d^7 intermediate $Rh_2(dmb)_4^{3+}$. This species homolytically abstracts an H atom from the organic substrate, producing the unstable $Rh_2(tmb)_4H^{2+}$ intermediate, which loses H^+ and an organic radical quickly. Subsequently a second H atom is abstracted to generate benzene. The authors argued that in comparison with H-abstraction in the excited $^3(d\sigma$–$d\sigma^*)$ state, for instance, which exhibit ns and μs lifetimes, electro-chemically generated d^8–d^7 complexes should proved more versatile.

The mechanism with which the electrolysis is poisoned by halocarbons, is believed to be the same as the H-abstraction one.

The $Ir_2(dmb)_4^{2+}$ complex can undergo two electrochemically reversible one-electron reduction processes at -1.34 and -1.53 V versus Ag/AgCl in 1.0 M KCI ($Ir_2(dmb)_4^{2+} + 1e^- = Ir_2(dmb)_4^+ / Ir_2(dmb)_4^+ + 1e^- = Ir_2(dmb)_4^0$) [55]. The reduction processes are accompanied by obvious and reversible UV–vis and IR spectral changes. The electro-generation of the $Ir_2(dmb)_4^0$ species allows reduction of CO_2 into either bicarbonate or formate [56].

Belonging to this same windmill family, the X-ray structure of the binuclear $Rh_2(tmb)_3(tmi)^+$ was reported, which was isolated from the bulk electrolysis of $[Rh_2(tmb)_4](CF_3SO_3)_2$ in acetonitrile. The Rh_2 distance is relatively short (2.970(1) Å) [58] in comparison with the parent dimers (Table 5). This complex was the first example of mixed-bridging ligand binuclear complex in this family.

Mann et al. also reported the synthesis of the mixed-ligand $Rh_2(dmb)_2(dppm)_2^{2+}$ (Fig. 7), which is prepared via a stoichiometric reaction between dmb and $[Rh(CO)Cl(dppm)]_2$ in methanol in the presence of NH_4PF_6 [59]. The X-ray structure reveals the expected face-to-face geometry, with two sets of *trans*-RhP_2, and RhC_2 fragments. The Rh…Rh distance is 3.161(1) Å, which is short in comparison with the Rh_2 data presented in Table 5. The authors attributed this distance to the shorter bite distance of dppm. The UV–vis spectra exhibit the characteristic low-energy $d\sigma^*$–$p\sigma$ band at 565 nm ($\varepsilon = 19\,800\ M^{-1}\ cm^{-1}$). This complex can be electrochemically oxidized via a first 1-electron process at $+0.70$ V, and a second 1-electron transfer at $+1.226$ V versus Ag/AgCl in CH_2Cl_2 containing 0.1 M of Bu_4NClO_4. The second process (3+ to 4+) is media dependent. When the electrolyte is Bu_4PF_6, the oxidation potential moves to $+1.728$ V versus Ag/AgCl. The key feature is the generation of the d^7–d^8 radical which was characterized by EPR and IR ($\nu(CN) = 2174\ cm^{-1}$). This radical has the tendency to disproportionate ($2d^7$–$d^8 = d^7$–$d^7 + d^8$–d^8), not to dimerize ($2d^7$–d^8 X tetramer).

This same group also prepared a new mixed-ligand complex $[Rh_2(dmb)_3(dppm)](PF_6)_2$ within a broader work aimed at understanding the disproportionation reactions in the d^7–d^8 oxidized intermediates and the effect of axial coordination and bridging ligand strain [60]. The following pairs have been investigated: $Rh_2(dmb)_4^{2+}/Rh_2(dmb)_2(dppm)_2^{2+}$; $Rh(dmb)_4^{2+}/Rh_2(tmb)_4^{2+}$; $Rh_2(tmb)_4^{2+}/Rh_2(tmb)_2(dppm)_2^{2+}$; $Rh_2(b)_4^{2+}/Rh_2(dppm)_2^{2+}$. Disproportionation of the d^7–d^8 tetrakis-diisocyanides species appeared greatly favored in contrast with the dppm-containing analogues. This lesser ability to disproportionate is associated with unfavorable enthalpic and entropic terms. The differences in the strong ability

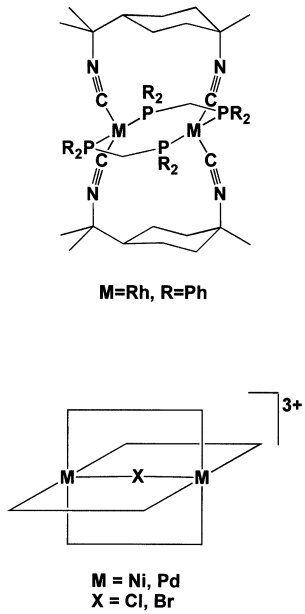

Fig. 7. Top: Molecular structure of the mixed-ligand $Rh_2(dmb)_2(dppm)_2^{2+}$ complex. Bottom: Encapsulation of Cl^- or Br^- ions by the windmill $M_2(dmb)_4^{4+}$ cations (M–Ni, or Pd) and dmb is drawn as squared U-shape ligands for clarity.

to bind axial ligands by the electro-generated d^7–d^7 complexes, determines the equilibrium constants. The d^7–d^7 dmb complexes are more destabilized than the tmb analogues because of ligand strain.

The second group in this windmill are the $Pd_2(dmb)_4^{2+}$ and $Ni_2(dmb)_4^{2+}$ complexes [23,32]. No X-ray structure is known so far for both complexes, but their chemical analyzes are consistent with the formulations $[Ni_2(dmb)_4](ClO_4)_4{\cdot}2H_2O$ [32] and $[Pd_2(dmb)_4](ClO_4)_4$ [23]. These species have the very strong tendency to encapsulate Cl^- and Br^- ions, which are confidently identified from chemical analyses, UV–vis spectroscopy, and molar conductivity in solutions. Despite these earlier works, no X-ray structure was still available. It is only in 1999 that Fortin obtained crystals of a species containing the $Pd_2(dmb)_4(\mu\text{-}Cl)^{3+}$ cation (Fig. 7) [61], issued from an unexpected redox reaction between the polymeric $[Pd_4(dmb)_5^{2+}(Cl^-)_2]_n$ material (discussed below) and neutral TCNQ. Gray's prediction was correct and the $Pd_2(dmb)_4^{2+}$ species did indeed encapsulated the Cl^- ion. The Pd–Cl distance is 2.7143(6) Å with a PdClPd angle of 180.0(1)°. The bite distance is 5.428 Å, and is the second longest one ever reported for dmb. For $Pd_2(dmb)_2(PPh_2Me)_4(\mu\text{-}Cl)^{3+}$, this distance is 5.536 Å [31]. Vibrational spectroscopy data are consistent with the centro-symmetric M–X–M structure for $Ni_2(dmb)_4(\mu\text{-}Cl)^{3+}$ with $\nu(NiCl) = 210$ (IR) and 284 cm^{-1} (R). High sensitivity of the samples to laser damage precluded Raman data to be obtained for the other complexes. The complementary IR data are as follow $Ni_2(\mu\text{-}Br)$, 158; $Pd_2(\mu\text{-}Cl)$, 201; $Pd_2(\mu\text{-}Br)$, 145 cm^{-1}.

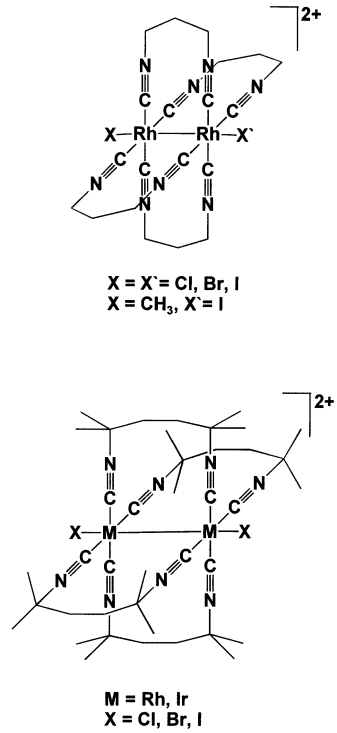

Fig. 8. Molecular geometries of the $Rh_2(b)_4(X)_2^{2+}$ (Top) and $Rh_2(tmb)_4(X)_2^{2+}$ species (bottom). Some dmb analogues are also known but not represented here.

The UV–vis spectra are characterized by a very intense and narrow absorption band at 306 (Pd) and 320 nm (Ni; $\varepsilon = 33\,000\ M^{-1}\ cm^{-1}$) for both $M_2(dmb)_4(\mu\text{-}Cl)^{3+}$ species, and are assigned to $^1A_{1g} \rightarrow {}^1A_{2u}$ (i.e. to a $d\sigma^*$ to $p_z + \pi^*$ (CNR) transition). EHMO computations for $Pd_2(dmb)_2(PPh_2Me)_4(\mu\text{-}Cl)^{3+}$ confirmed this assignment and place this band at 344 nm [32]. At 20 K, $Ni_2(dmb)_4(\mu\text{-}Cl)^{3+}$ in poly(methylmethacrylate) films exhibits two vibrational progressions in the UV–vis spectra, with spacings of 436 and 2174 cm^{-1}. The modes are readily identified as ν(NiC) and ν(C≡N), respectively, and strongly imply that the electronic transition involves M to π^* (CNR) change transfer.

Reactions of the $Ni_2(dmb)_4(\mu\text{-}X)^{3+}$ complex with I_2 generates the mixed-valent and paramagnetic complexes $[Ni_2(dmb)_4(\mu\text{-}X)](I_3)_4$ (X = Cl, Br) [32]. The IR ν(NiX) data are 228 (Cl) and 165 cm^{-1} (Br) (Table 7).

3.6. The d^7-d^7 $M_2(diiso)_4$ complexes

These compounds are isoelectronic to the $M_2(CO)_{10}$ complexes (M = Mn, Tc, Re), and are also structurally related to them. Only complexes of Rh(II) and Ir(II) have been confidently characterized (Fig. 8) [42,54,59,62–64]. The complexes

exhibit a M–M single bond ranging from about 2.8 to 2.9 Å (Table 8), and Raman and resonance spectroscopy established the presence of an intense $\nu(M_2)$ scattering in the 88–176 cm^{-1} range. The $\nu(M_2)$ values vary as I < Br < Cl as expected for species exhibiting the linear X–M–M–X structure. For the lighter axially substituted $Rh_2(tmb)_2(tmb)_2(OH_2)_2^{4+}$, this value was the highest (176 cm^{-1}), while for the $Ir_2(tmb)_4H_2^{2+}$ dimer, $\nu(Ir_2)$ is not the highest (136 cm^{-1}) because the Ir_2 bond distance is the longest (2.920 Å) [42]. The UV–vis spectra exhibit the intense and characteristic $d\sigma-d\sigma^*$ absorption in the 310–400 nm range for the Rh_2 species, and is found in the 270–320 nm window for M = Ir. λ_{max} is also X–dependent with $H_2O < Cl < Br < I$. The exception is the $Rh_2(b)_4H^{3+}$ complex, where $\lambda(d\sigma^*-p\sigma) =$ 549 nm. To our knowledge these species do not luminesce at room temperature, either in solutions, or in the solid state.

4. Trinuclear species

4.1. The linear species

The first spectroscopic evidence of linear trinuclear species of $Rh(CNR)_4^+$ species appeared in 1975 [34]. The UV–vis technique was used to extract the extinction coefficients and the formation constants. These species are characterized by an absorption band in the 610 to 730 nm range with ε of about 10 500–16 900 M^{-1} cm^{-1}.

These features are interpreted in terms of an electronic transiton arising from weak M…M interactions between the occupied $a_{1g}(d_{z2})$ and the unoccupied $a_{2u}(p_z,\pi^*(CNR)$ orbitals, in the dimer, and $2a_{1g}-2a_{2u}$ in the trimer [33]). These trinuclear species do not luminesce at room temperature, but transient absorption spectroscopy established that the excited state lifetime of the $^3A_{2u}$ state, $^3(d\sigma^*-p\sigma)$,

Table 7
Room temperature photophysical data for d^8–d^8 $M(CNR)_4^+$ [a]

Complexes	λ_{fluo} (nm)	τ_e (ns)	ϕ_e	λ_{phos} (nm)	τ_e (μs)	Reference
$Rh_2(CN\text{-}p\text{-}tol)_8^{2+}$	697	<2	0.0065			[36]
$Rh_2(b)_4^{2+}$	656	1.2	0.056	830	8.5	[36,48]
$Rh_2(4\text{-}b)_4^{2+}$ [a]	634	?	0.077			[39]
$Rh_2(tmb)_4^{2+}$	614	0.2	0.046	770	0.025	[48]
		0.90	0.055		0.030	[43]
$[Rh_2(dmb)_4](PF_6)^2$	550			660		[43]
$[Rh_2(dmb)_4](TFBP)_2$ [b]	562					[43]
$[Rh_2(dmb)_4](BPh_4)_2$	587			700		[43]
$[Ir_2(tmb)_4](BPh_4)_2$	735	<2	0.0025	1080	0.21	[44]

[a] Only selected room temperature data are included for solutions. The 77 K data can be found in the references therein.

[b] $Ir_2(dmb)_4^{2+}$ also fluoresces at 710 nm [6].

Table 8
Selected structural and spectroscopic data for d^7–d^7 complexes

Complexes	$d(M_2)$ (Å)	$\nu(M_2)$ (cm^{-1})	$\lambda_{max}(d\sigma\text{-}d\sigma^*)$ (nm) (ε M^{-1} cm^{-1})	Reference
$Rh_2(CN\text{-}p\text{-}tol)_8I_2^{2+}$	2.785			[63]
$Rh_2(b)_4Cl_2^{2+}$	2.837	130	342 (52000)	[62,65]
$Rh_2(b)_4Br_2^{2+}$		107	364 (68500)	[62]
$Rh_2(b)_4I_2^{2+}$		88	397 (62000)	[62]
$Rh_2(b)_4(CH_3)I^{2+}$			397	[62]
$Rh_2(b)_4(H)^{3+}$			549 + 0.1 M p-tolSO_3H	[62]
$Rh_2(tmb)_4(OH_2)_2^{2+}$		176	311 (in 1 M H_2SO_4)	[62]
$Rh_2(tmb)_4Cl_2^{2+}$	2.837	155	333 (55500)	[62,64]
$Rh_2(tmb)_4Br_2^{2+}$		115	360 (60000)	[62]
$Rh_2(tmb)_4I_2^{2+}$			394 (55200)	[62]
$Rh_2(dmb)_4Cl_2^{2+}$			337 (55000)	[57]
$Rh_2(dmb)_4Br_2^{2+}$	2.9		368 (55500)	[57]
$Rh_2(dmb)_2(dppm)_2Cl_2^{2+}$			402 (30000)	[59]
$Ir_2(tmb)_4Cl_2^{2+}$		140	274 (50500)	[62]
$Ir_2(tmb)_4Br_2^{2+}$		128	297 (52600)	[62]
$Ir_2(tmb)_4I_2^{2+}$	2.803	116	330 (49800)	[62,64]
$Ir_2(tmb)_4(H)_2^{2+}$	2.920	136	320 (17000)	[42]

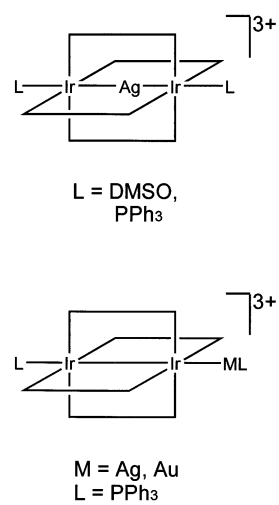

Fig. 9. Linear structures of the hetero-trinuclear clusters $Ir_2Ag(dmb)_4(PPh_3)_2^{3+}$ and $Ir_2(dmb)_4(PPh_3)$-$(MPPh_3)_2^{3+}$. The dmbs are shown as squared U-shape ligands for clarity.

is 0.14 μs at room temperature for $[Rh_3(CNC_6H_4Me)_{12}]^{3+}$ [36]. Unfortunately, no X-ray structure was reported on the $(d^8)_n$ species. Balch et al. have reported during the same year the preparation and structure of the related M–M bonded trinuclear

$Pd_3(CNMe)_6(PPh3)_2^{2+}$ cluster [65]. This cluster is linear and the Pd–Pd bond length is short (2.5921(5) Å). The $\nu(Pd_2)$ scatterings are found at 132 (IR) and 90 cm^{-1} (Raman) [66]. However no homonuclear '$M_3(diiso)_x$' species is known so far.

Mann et al. reported the syntheses and X-ray structures of the encapsulated species $Ir_2Ag(dmb)_4L_2^{3+}$ clusters (L = DMSO [6], PPh_3 [67]), and linear $Ir_2(dmb)_4(PPh_3)(MPPh_3)^{3+}$ clusters (M = Ag, Au) [7]. These clusters exhibit the windmill structure (Fig. 9). Both adducts of the encapsulated species, L = DMSO and PPh_3, exhibit identical Ir–Ag distances of 2.642(1) Å, placing the bite distance at 5.284 Å. The $Ir_2Ag(dmb)_4^{3+}$ cluster is prepared from direct addition of $AgPF_6$ to the starting material $Ir_2(dmb)_4^{2+}$. The latter exhibits the ability of coordinating ligands in the axial positions. Adducts of pyridine, PPh_3, and DMSO are reported, and the UV–vis spectra reveal a strong absorption at 390 nm that is strongly sensitive to the nature of these ligands. This cluster emits in CH_2Cl_2 solution at room temperature ($\lambda_{emi} = 640$ nm; $\tau_e = 3.6$ μs), but also photo-induced elimination of the Ag^+ ion (as $Ag(NCMe)_4^+$) is observed. This elimination is reversed in the dark. The Ir^+ ions act as Lewis bases, while Ag^+ is a Lewis acid, and contrast with the Pd–Cl–Pd species described above, where the Cl^- is the Lewis base, the Pd^{2+} metals, the Lewis acids.

The $Ir_2(dmb)_4(PPh_3)(MPPh_3)^{3+}$ complexes (M = Ag, Au) are prepared differently where the heteronuclear metal ion is incorporated as $M(PPh_3)_2^+$ (M = Ag, Au). Encapsulation of the bonded $[M–PPh_3]^+$ species is impossible. The IR data for ν(C≡N) indicate that the two Ir atoms are not equivalent. For M = Au, X-ray data reveal bonding (d(AuIr) = 2.607(2) Å). The Ir…Ir separation is on the other hand, somewhat short (2.986(2) Å), in comparison with the data provided in Table 5 for $Ir_2(dmb)_4^{2+}$ species (3.601, 3.944, and 4.415 Å, depending on the counter ion). The UV–vis spectra are characterized by an absorption at 380 and 400 nm, for M = Au and Ag, respectively, and are assigned to $2a_1–3a_1$ based upon a Ir–Ir–M model with a strong Ir–M bond (i.e. dσ–dσ* in the Ir–M mainfold).

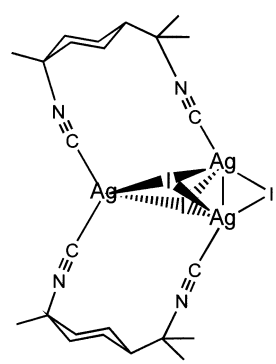

Fig. 10. Cluster geometry for $Ag_3(dmb)_2I_3$.

4.2. The cyclic complexes

To our knowledge only one species is known. The crystallographically characterized $Ag_3(dmb)_2I_3$ complex was reported in the light of mechanism on formation of $Ag_2(dmb)_2X_2$ species (X = Cl, Br, I) discussed earlier [68]. The structure consists of a $Ag(\mu\text{-}I)_3Ag$ fragment bridged by the pincer residue $Ag(dmb)_2^+$ (Fig. 10). The Ag…Ag separation in the triply-I bridged fragment is very short (2.805(4) Å), and Raman data for $\nu(Ag_2)$ (122 cm^{-1}) suggest weak M_2-interactions equivalent to half of a single bond.

On the other hand, the remaining Ag metal, which is bridged by two dmb and two I ligands, exhibit non-bonding Ag…Ag distances of 3.633(4) and 3.760(4) Å. All three Ag atoms are tetracoordinated. The UV–vis spectra are characterized by a weak, a medium, and strong absorptions at 320, 280, and 250 nm, respectively, and resemble that of the $Ag_2(dmb)_2(I)_2$ analogue [19].

5. Tetranuclear species

5.1. The linear complexes

For the briefly mentioned H_2 evolution reactivity in the Rh species, one of the key species turned out to be a tetranuclear complex formed with two $Rh_2(b)_4^{2+}$ dimers [69–71]. Indeed when $Rh_2(b)_4^{2+}$ reacts with HCl, it produces species of the type $(1/n)[Rh_2(b)_4Cl^{2+}]_n + 1/2H_2$ [3,11]. One of the species is $[Rh_2(b)_4]_2^{6+}$ (λ_{max} = 558 nm) which can photochemically reduce the Fe^{3+} ion to form the oxidized d^7–d^7 $Rh_2(b)_4^{4+}$ dimer and Fe^{2+}. The identity of the tetranuclear $[Rh_4(b)_8Cl]^{5+}$ was formally made using X-ray data revealing two $Rh_2(b)_4$ moieties linked by a Rh–Rh single bond (2.775(4) Å). The Rh…Rh distances inside the $Rh_2(b)_4$ residues are 2.932(4) and 2.923(3) Å. The Cl^- anion linearly bridges two Rh_4 units (d(Rh–Cl) = 2.613(8) and 2.643(9) Å) to form an infinite chain in the solid state. There is a near perfect eclipsed face-to-face conformation within the $Rh_2(b)_4$ units, but the bonded $Rh_2(b)_4$–$Rh_2(b)_4$ fragments are not eclipsed. The strong absorption at 600 nm has been assigned to a $d\sigma$–$d\sigma^*$ transition within the linear Rh_4^{6+} unit [72]. In addition, using electrochemical methods, Mann and Parkinson [73] demonstrated that $[Rh_4(b)_8]^{6+}$ binds with the Cl^- anion to form the known $[Rh_4(b)_8Cl]^{5+}$ cation in solutions. Other species such as $Rh_4(b)_8Cl_2^{4+}$ and $[Rh_2(b)_4^{3+}]_2$ were spectroscopically identified from UV–vis titration experiments [2], but no X-ray structures are yet available.

Despite the presence of steric Me groups, $Rh_2(tmb)_4^{2+}$ reacts cleanly with $Rh_4(b)_8^{6+}$ to form $Rh_2(tmb)_4Rh_4(b)_8^{8+}$ [74]. These species are characterized by absorptions at 780, 980, and >1300 nm bands. Based upon the very low energies of these bands, oligomeric structure similar to that found in $Rh_4(b)_8Cl^{5+}$ is suspected. Larger species such as $Rh_2(tmb)_4/Rh_4(b)_8/Rh_2(tmb)_4^{10+}$ and $[Rh_2(tmb)_4$-$Rh_4(b)_8]_2^{16+}$ have also been postulated on the basis of titration measurements [74]. An overview of the mechanistic aspect of the photo-induced H_2 evolution reaction

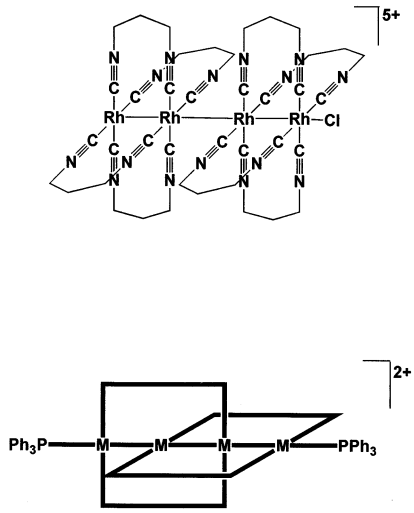

Fig. 11. Structures of the linear homonuclear M–M bonded M_4 species; Top: $Rh_4(b)_8(X)^{5+}$ (the solid state structure consists of an infinite chain of this repetitive unit); Bottom catenate $M_4(dmb)_4L_2^{2+}$ (M = Pd, Pt).

Table 9
Structural and spectroscopic data for the $M_4(dmb)_4(PPh_3)_2^{2+}$ clusters [76,77]

Data	M = Pd	M = Pt
$d(M–M)_{inner}$ (Å)	2.524(10)	2.641(2)
$d(M–M)_{outer}$ (Å)	2.534(10)	2.666(2)
dmb bite distance (Å)	5.06	5.30
$<M_3$ (°)	174.5(2)	175.8(1)
d(MP) (Å)	2.35(2)	2.33(1)
twist angle (°)	82.7	74.7
$\nu(M–M)_{sym.}$	165	162
$\nu(M–M)_{assym.}$	86	84
$\lambda_{max}(d\sigma \rightarrow \delta\sigma^*)$ (nm) [a]	538	405
$\varepsilon(d\sigma \rightarrow d\sigma^*)$ M^{-1} cm^{-1} [a]	53700	35800
λ_{emi} (nm) (77 K) [a]	684	750
τ_e (μs) (77 K) [a]	0.67	0.0027

[a] In ethanol.

has been presented by Gray et al. [75], and this shows how the linear tetranuclear species are involved in the reactions. The UV–vis spectra are dominated by a strong and narrow $d\sigma–d\sigma^*$ absorption between 550 and 620 nm, depending upon medium and coordinating ligands [72].

More recently our group reported the preparation and the X-ray structures of the linear $M_4(dmb)_4(PPh_3)_2^{2+}$ clusters (M = Pd, Pt) [76,77]. Their syntheses proceed as follows:

$$2M_2(dba)_3{\cdot}CHCl_3 + dmb(excess) + 2PPh_3 \rightarrow M_4(dmb)_4(PPh_3)_2^{2+} + \text{other products} \quad (3)$$

The presence of $CHCl_3$ (or a halocarbon, or mild oxidating agent) is crucial to this reaction. Indeed $CHCl_3$ oxidizes the M atoms to a formal oxidation state of 0.5. In the absence of PPh_3, the polymeric material $[M_2(dmb)_5^{2+}]_n$ is formed (M = Pd, Pt), and confidently identified. The structure consist of a quasi-linear M–M bonded P–M_4–P unit exhibiting a catenate (Fig. 11). The two main features are that these complexes are the first 58-electron linear clusters for both Pd and Pt, and that catenate is observed for the diisocyanide ligands. Selected structural data and spectroscopic data are compared in Table 9. Formal M–M bonds are depicted from X-ray studies, and $\nu(M_2)$ are found strong in the FT-Raman spectra at 162 and 165 cm^{-1}, and at 84 and 86 cm^{-1} for M = Pd, and Pt, respectively. A strong and narrow $d\sigma^*$–$d\sigma^*$ band is also evident at 538 and 405 nm for M = Pd and Pt, respectively. Both clusters are luminescent at 77 K in glassy solutions in the 700 nm range. However, τ_e is 670 ns for the Pd_4 complex which is significantly longer than that found for Pt_4(τ_e = 2.7 ns). The ns scale is not unprecedented for such species as τ_e ranges between 71 and 177 ns for the $Pd_2(diiso)_2X_2$ species presented in Table 4. Non-rigidity, excited state homolytic M–M bond cleavage, and L- or X-photo-induced lability are all parameters that contribute in the competitive non-radiative processes, hence decreasing τ_e and ϕ_e. No electrochemical measurements has been performed in order to estimated the excited state redox potentials for these species.

The first heteronuclear tetrametallic clusters of these diisocyanide ligands have reported by Mann et al. and are of the general formula $Rh_2(diiso)_4(M(CO)_4L)_2^{2+}$ with M = Mn, Re, diiso = b, and tmb, and L = CO, and PPh_3 [78,79]. The preparation consists in a sunlight or lamp (Hg vapor) irradiation of the $Rh_2(diiso)_4^{2+}$ species in the presence of $Mn_2(CO)_{10}$, $Re_2(CO)_{10}$, or $Re_2(CO)(PPh_3)_2$. The X-ray structure for $Rh_2(tmb)_4(Mn(CO)_5)_2^{2+}$ (Fig. 12) consists of a $Rh_2(tmb)_4$ fragment axially bonded to two $Mn(CO)_5$ moieties. None of the $Mn(CO)_4$ and $Rh(CN)_4$ are eclipse due to steric reasons. The twist angles range from 25 to 31°. The Rh…Rh distance is somewhat slightly long (2.922(2) Å) in comparison with

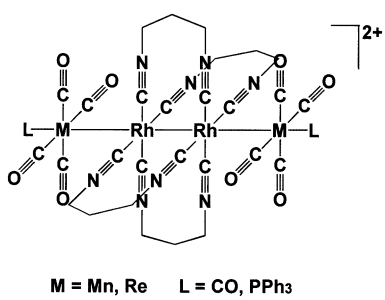

Fig. 12. Structure of the M–M′ bonded complexes $Rh_2(b)_4(M(CO)_4L)_2^{2+}$.

data for d^7–d^7 species (2.837 Å), but clearly shorter than that found for the d^8–d^8 starting $Rh_2(diiso)_4^{2+}$ (3.262 Å), indicating the presence of some Rh–Rh bonding. The Rh–Mn bond lengths are 2.905(5) and 2.883(4) Å, and are somewhat close to that of $Mn_2(CO)_{10}$ (2.923(3) Å) [80], and formal bonding may readily be anticipated. The UV–vis spectra exhibit a strong absorption in the 560–640 nm range with $55800 < \varepsilon < 106000\ M^{-1}\ cm^{-1}$. These bands have been assigned to a fully delocalized $d\sigma$–$d\sigma^*$ transition along the M–Rh–Rh–M frame [79]. Irradiation of these species at 632.8 nm leads to no net photochemistry, but in the presence of O_2 or traces of H_2O, decomposition occurs [79]. The mixed valence species $Rh_2(tmb)_4(Re(CO_5))_2^{3+}$ can be electro-generated from the corresponding dication in acetonitrile, and has been characterized by EPR and IR spectroscopy [81]. However upon further oxidation, one of the Rh–Re bond cleaves and the trimetallic fragment $Rh_2(tmb)_4(Re(CO)_5)^{3+}$ is generated along with the side product $Re(CO)_5(NCMe)^+$. This trinuclear cluster can undergo a 2-electron reduction resulting in the formation of $Rh_2(diiso)_4^{2+}$ and $Re(CO)_5^-$. The Mn analogue experiences a net 2-electron oxidation to form $Rh_2(tmb)_4(Mn(CO)_5)_2^{4+}$, which upon further oxidation generates $Rh_2(diiso)_4^{4+}$ and $Mn(CO)_5(NCMe)^+$. The trinuclear intermediate $Rh_2(tmb)_4$-$(Mn(CO)_5)^{3+}$ was only observed transiently via fast-scan cyclic voltammetry. The 2-electron reduction of both $Rh_2(tmb)_4(M(CO)_5)_2^{2+}$ clusters (M = Mn, Re) yields $Rh_2(diiso)_4^{2+}$ and $M(CO)_5^-$. Upon re-oxidation conditions, this process is found completely reversible [81].

5.2. The non-linear complexes

The preparation of the non-linear M_4 species can be achieved using mixed-ligand and mixed-metal conditions. For instance, the tetranuclear complex $[Ag_4(dmb)_4(TCNQ)_3](TCNQ)$ (Fig. 13) is synthesized from the template $[Ag_2(dmb)_2](ClO_4)_2$ material and LiTCNQ [21]. The structure consists of two cyclic $Ag_2(dmb)_2^{2+}$ units bridged by three $TCNQ^-$ via weak N…Ag interactions. The bridging TCNQ groups are placed face-to-face in a stair-shaped geometry promoting some π-interactions. The interplanar TCNQ…TCNQ distance is 3.372 Å, and the Ag…Ag separaction is 4.115(8) Å. Two of the N atoms, are bridging two Ag metals, and two of the Ag cations adopt a distorted tetrahedral coordination, in

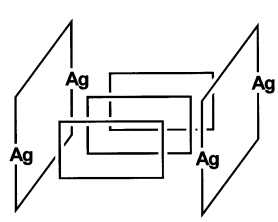

Fig. 13. Scheme showing the stairway configuration of the $TCNQ^-$'s (represented by rectangles) between two $Ag_2(dmb)_2^{2+}$ units.

order to promote bridging of the three TCNQ moieties with four Ag centers. The CAgC angles are 140.3(2) and 147.4(2)°, which are large in comparison with the ideal tetrahedral angle, and are the result of weak Ag^{+}…$TCNQ^{-}$ bondings. The most interesting feature is the parallel stacking of these Ag_4 species in the solid state, placing adequately the π-TCNQ system for electronic and magnetic communications. The material behaves as extended chains of antiferromagnetically coupled $S = 3/2$ (bridged $TCNQ^{-}$) and $S = 1/2$ (free counter anion) centers. No hyperfine structure was observed between 106 and 290 K, indicating the presence of rapid exchange in the paramagnetic system.

Reaction of $Ni(O_2CMe)_2$ with tmb in methanol in the presence of $NaBPh_4$ affords the paramagnetic tetranuclear complex $[Ni(OMe)_4(O_2CMe)_2(tmb)_4]^{2+}$ (Fig. 14) [82]. This compound adopts a cubane structure for the $Ni_4(OMe)_4$ core. The O_2CMe ligands bridge two opposite faces of the cube, and the 4 tmb ligands bridge the four remaining faces. The approximate geometry is D_{2d}. The Ni…Ni distances range from 3.0 to 3.2 Å, and the Ni–O bond lengths are in the order of 2.05 ± 0.02 Å. Magnetic susceptibility measurements show that the compound exhibit a diamagnetic ground state.

In an attempt to prepare a M–M bonded oligomer containing six linearly placed metal atoms, the $Pt_4(dmb)_4^{2+}$ cluster and Au-containing fragments were used [83]. The reaction between $Pt_2(dba)_3{\cdot}CHCl_3$, $[Au(PPh_3)_2](PF_6)$ and dmb in excess produced unexpectedly $(PPh_3)AuCl$, $Pt_2(dmb)_2Cl_2$, $[Pt_4(dmb)_5(PF_6)_2]_n$, and the heteronuclear cluster $[Pt_2Au_2(dmb)_2(PPh_3)_4](PF_6)_2$ (Fig. 15) [83]. The green cluster was identified crystallographically. The structure consists of a flattened butterfly $Pt_2Au_2^{2+}$ core exhibiting a formal Au^0–Au^0 bond as the edge sharing segment ($d(Au_2) = 2.5977(6)$ Å). The Au–Pt bond lengths are 2.8422(5) and 2.8082(5) Å. The Pt atoms bridged by two dmb ligands, forming a large ring structure that encircles the Au–Au bond. The bite distance is 5.02 Å. Finally, each metal atom bears a PPh_3 ligand placed in-plane with respect to the Pt_2Au_2 frame. The Raman data for $\nu(Au_2)$ and $\nu(PtAu)$ are 121 cm^{-1}, and 100 and 85.5 cm^{-1}, respectively. The UV–vis spectra are characterized by a series of narrow absorptions (ε in parentheses) at 316 (32300), 366 (37800), 418 (21500), 516 (2860), and 655 nm (834 M^{-1}

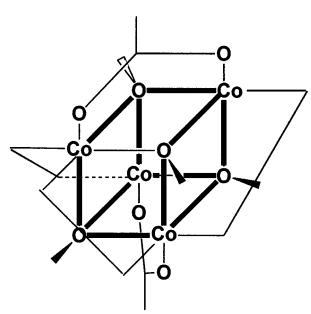

Fig. 14. Scheme showing the cubane structure of the tetranuclear complex $Co_2(OMe)_4(tmb)_4(O_2CMe)_2^{2+}$. Only 3 of the 4 tmb ligands are shown for clarity. Here the tmb ligands are drawn as squared U-shape ligands.

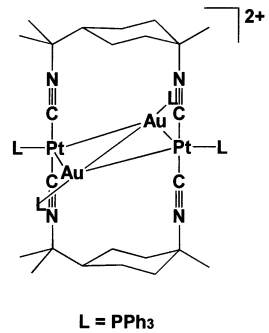

Fig. 15. Flattened butterfly geometry of the heteronuclear cluster $Pt_2Au_2(dmb)_2(PPh_3)_4^{2+}$.

cm^{-1}). The cluster is luminescent at low temperatures both in frozen glasses and in the solid state ($\lambda_{emi} = 875$ nm; $\tau_e = 4.4 \pm 0.4$ ns, in butyronitrile at 77 K). The emission band appears asymmetric with a low energy shoulder at a spacing of 560 cm^{-1}. A PtAu to π*(CNR) charge transfer assignment might be appropriate in this case, in the light of the EHMO calculations.

6. The polymeric materials

6.1. Polymers with tmb

Dartiguenave, Beauchamp et al. reported two crystallographic investigations on polymers formed when an Ag salt reacts with tmb [84,85]. Using AgX ($X = ClO_4^-$, BF_4^-, NO_3^-, PF_6^-), polymers having the formula $[Ag_2(tmb)]_3 \cdot (ClO)_4 \cdot [Ag_2(tmb)]_3 \cdot (PF_6)_2 \cdot 2MeCN$, $Ag(tmb)NO_3$ and $Ag(tmb)BF_4$ have been prepared and characterized. The $Ag_2(tmb)_3^{2+}$ materials consist of two $[Ag(tmb)^+]_n$ chains placed side by side with the Ag atoms pointing toward each other. The two chains are crossed linked with another tmb ligand at every step, joining a Ag atom from one chain to the corresponding one on the opposite chain. The authors compared this structure to an infinite ladder (Fig. 16). In addition, each Ag atom forms a weaker contact with the counter ClO_4^- (d(Ag…O) = 2.73(1) Å) and PF_6^- anions (d(Ag…F) = 2.873(6) Å). Within the space created by the ladder structure, the PF_6^- material allows two MeCN solvent molecules to stack inside the $Ag_4(tmb)_4^{4+}$ loops. Both crystal systems are triclinic ($P\bar{1}$) and the unit cell volume for the PF_6^- material is indeed slightly larger ($Z = 1$; 1122.8 $Å^3$ for ClO_4^-, 1172 $Å^3$ for PF_6^-). In contrast, the $[Ag(tmb)(BF_4)]_n$ polymer forms a large zig-zag structure (Fig. 16), where the C–Ag–C co-ordination is quasi-linear, allowing some contact with the BF_4^- anion (d(Ag…F) = 2.850(11) Å). The zig-zag structure is induced by the presence of two conformations that tmb adopts. No Ag…Ag interactions are depicted in the structure. The $[Ag(tmb)(NO_3)]_n$ structure greatly differs from the two former, in part, because of significant $Ag^+ \ldots NO_3^-$ interactions (d(Ag–O) = 2.519(5) and

2.647(5) Å), as evidence by the smaller C–Ag–C angle (144.9(2)°). The structure consists of an infinite $[Ag(tmb)^+]_n$ chain forming a smaller zig-zag. These three different structures find their origins from the various conformations that tmb may adopt, and the Ag…counter anion interactions.

6.2. Polymers with dmb

The reaction of AgX salts ($X = BF_4^-$, PF_6^-, NO_3^-, ClO_4^-) with an excess of dmb afford crystalline materials that analyze as $[Ag(dmb)_2X]$. These materials are isostructural (Table 10), except for the NO_3^- material which is found to be crystallize with some water molecules held by H-bonds [8,18,86,87]. All these

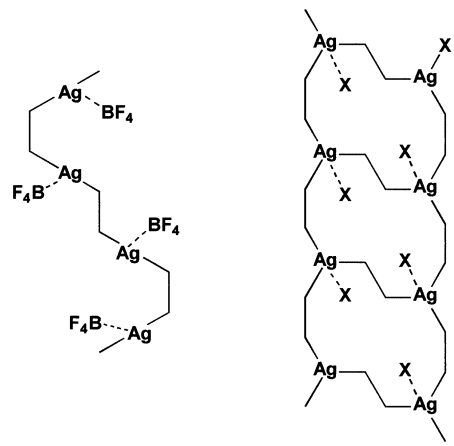

Fig. 16. Segment view of the zig-zag $[Ag(tmb)^+]_n$ (left) and ladder-shaped $[Ag_2(tmb)_3^+]_n$ polymers (right). The $Ag^+…BF_4^-$ interactions occur via $Ag^+…F$ contacts. The CN and methyl groups of the tmb ligands are not drawn for clarity.

Table 10
Structural comparison in the $\{Ag(dmb)_2^+\}_n$ polymers [a]

Polymers	d(Ag…Ag) (Å)	∠Ag_3 (°)	Reference
$\{[Ag(dmb)_2]TCNQ{\cdot}2THF\}_n$	5.2829(6)	139.25(2)	[87]
$\{[Ag(dmb)_2]TCNQ{\cdot}1.5TCNQ°\}_n$	5.2787(11)	132.96(3)	[87]
$\{[Ag(dmb)_2]DCTC\}_n$	5.203(6)	139.85(7)	[87]
	5.156(6)	139.85(7)	
$\{[Ag(dmb)_2]NO_3{\cdot}0.7H_2O\}_n$	5.1884(6)	139.88(1)	[18]
$\{[Ag(dmb)_2]TCNQ{\cdot}CH_2Cl_2\}_n$	5.065(3)	140.36(1)	[86]
$\{[Ag(dmb)_2]PF_6\}_n$	4.964(1)	139.15(4)	[8]
$\{[Ag(dmb)_2]BF_4\}_n$	4.9557(9)	140.46(2)	[18]
$\{[Ag(dmb)_2]ClO_4\}_n$	4.9496(1)	139.57(2)	[18]
$\{[Ag(dmb)_2]TCNQ\text{-}0.5TCNQ°{\cdot}0.5C_7H_8\}_n$	4.8816(4)	139.71(3)	[87]

[a] Only U-shape dmb polymers are listed.

materials crystallize as long and narrow needles, and crystallography reveals the presence of parallel stacked quasi-1D materials somewhat like rigid sticks. All the Ag atoms are tetrahedrally coordinated in a distorted fashion and doubly bridged with each of the two adjacent Ag neighbors by dmb ligands (Fig. 17). The dmb ligands, which adopts the *syn* configuration (U-shape), are mostly all unidirectional oriented head-to-tail, probably due to steric reasons [8]. The Ag…Ag separations are generally found to be about 5 Å, a distance that is too large for Ag…Ag interactions. The Ag_3 angle is 140° in most cases (Table 10). The flexibility of the dmb ligand has clearly been demonstrated in the dimeric and tetrameric species, but despite the presence of steric hindrance, this flexibility is also felt within the polymers as the Ag…Ag separations vary between 4.88 to 5.28 Å. As depicted in Table 10, the counter anion can easily be exchanged, notably with $TCNQ^-$ [86,87]. This polymer can crystallize either with CH_2Cl_2 or 2THF crystallization molecules. In addition, doping with a certain amount of neutral TCNQ also afford crystals of suitable quality for structure analysis [87]. So far, nine structures exist on these polymers.

The Cu analogues have also been prepared from the direct reaction of $[Cu(NCCH_3)_4](BF_4)$ with dmb, or from $Cu(BF_4)$ with dmb in excess. In the latter case, dmb acts as both reducing agent and bridging ligand. No crystal suitable for crystallography was obtained [18]. The materials appear under different morphology (amorphous, semi-crystalline, and crystalline) depending on the synthesis methodology. The isostructurallity between the two metals was clearly established from X-ray powder diffraction patterns. Such investigation subsequently led to the preparation of mixed-metal polymers $\{[Ag_xCu_{1-x}(dmb)_2]BF_4\}_n$ (Table 11) [88].

The X-ray powder diffraction peaks proved narrow and the 2-theta values are intermediate between data collected for the pure homometallic materials. This result suggests that the two metals (Cu, and Ag) are randomly distributed along the polymer chains.

The molecular weight averaged in weight (M_W) is 156 000 for the semi-crystalline $\{[Cu(dmb)_2]BF_4\}_n$ polymer according to light scattering measurements [18], corresponding to 300 units and a 0.11 μm long polymer. Osmometric measurements indicate that the molecular weight averaged in number (M_n) is 133 000, correspond-

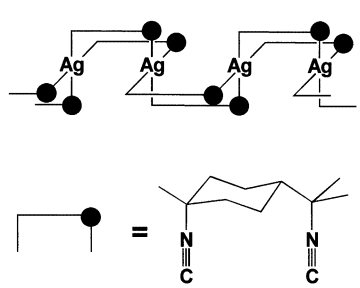

Fig. 17. Structure of a segment of the $\{[Ag(dmb)_2]^+\}_n$ polymer. The coordination around the Ag atom is tetrahedral.

Table 11
X-ray powder pattern indexation data for the $\{[Ag_xCu_{1-x}(dmb)_2]BF_4\}_n$ polymeric materials [a]

%Ag	%Cu	*a*	*b*	*c*
0	100	21.88	13.29	9.72
5	95	21.72	13.25	9.64
20	80	21.84	13.32	9.59
50	50	21.76	13.49	9.48
65	35	21.35	13.52	9.65
100	0	22.10	13.67	9.52
		(22.27)	(13.77)	(9.42)

[a] The values in brackets are the X-ray data for a single crystal analysis. The relative uncertainties can be taken as the differences between the X-ray powder data and these data [88].

ing to an indice of polydispersity of 1.17 (M_W/M_n). These same measurements also indicated that the amorphous materials exhibit the larger M_n. For instance, M_n for the amorphous $\{[Cu(dmb)_2]BF_4\}_n$ polymer is 140 000. In contrast, these same techniques (light scattering, and osmometry) indicated that the Ag polymers were of 10 000 or less (i.e. oligomers of 10 to 12 units). In all cases, the lack of solubility proved an obstacle and the use of other techniques was fruitless. Spin lattice relaxation time measurements (T^1) by ^{13}C-NMR were performed assuming that relaxation was governed by dipole–dipole interactions, in order to get some insight on the relative dimensions and molecular motions in solutions of the polymers. The probed ^{13}C is C # 2 (Fig. 18), and the mononuclear $[M(CN\text{-}t\text{-}Bu)_4](BF_4)$ complexes (M = Ag, Cu), are used for comparison purposes. Qualitatively T_1 is clearly function of the size of the tumbling molecules, and correlation times have been extracted. The great difference in M_W data between the Cu and Ag polymers were rationalized in term of greater lability of the ligands on the Ag(I) metals.

Lebrun has recently prepared new rigid stick 1D materials using a new strategy in order to change the M…M separations within the polymer chain [88]. Indeed, using the convenient tetrahedral coordination behavior of the Cu(I) and Ag(I) metals in $Cu_2(dppm)_2(NCMe)_4^{2+}$ and Ag $(dppm)_2^{2+}$, these dimers are reacted with a slight excess of dmb affording a weakly soluble polymeric material $\{M_2(dppm)_2(dmb)_2^{2+}\}_n$ (M = Ag, Cu). Crystallography was used to prove the structure for the Ag polymer, which consists of $Ag_2(dppm)_2^{2+}$ units doubly bridged by dmb ligands adopting the *Z*-conformation (Fig. 19). The Ag atoms are tetra-coordinated in a distorted fashion, by two P atoms, and two CN groups. The *Z*-conformation was used by the ligand in order to minimize intramolecular unfavorable steric interactions. The Ag…Ag distances are 4.028 and 9.609 Å, for the dppm and dmb fragments, respectively. The Cu analogue turned out isostructural according to X-ray powder patterns, but significantly more amorphous.

Both series of $\{[M(dmb)_2]Y\}_n$ polymers (M = Ag, Cu; $Y = BF_4^-$, PF_6^-, NO_3^-, ClO_4^-, $TCNQ^-\cdot x TCNQ^0$) exhibit second order phase transitions between 35 and 150°C associated to a glass transition. The glass transition temperature (T_c) is not

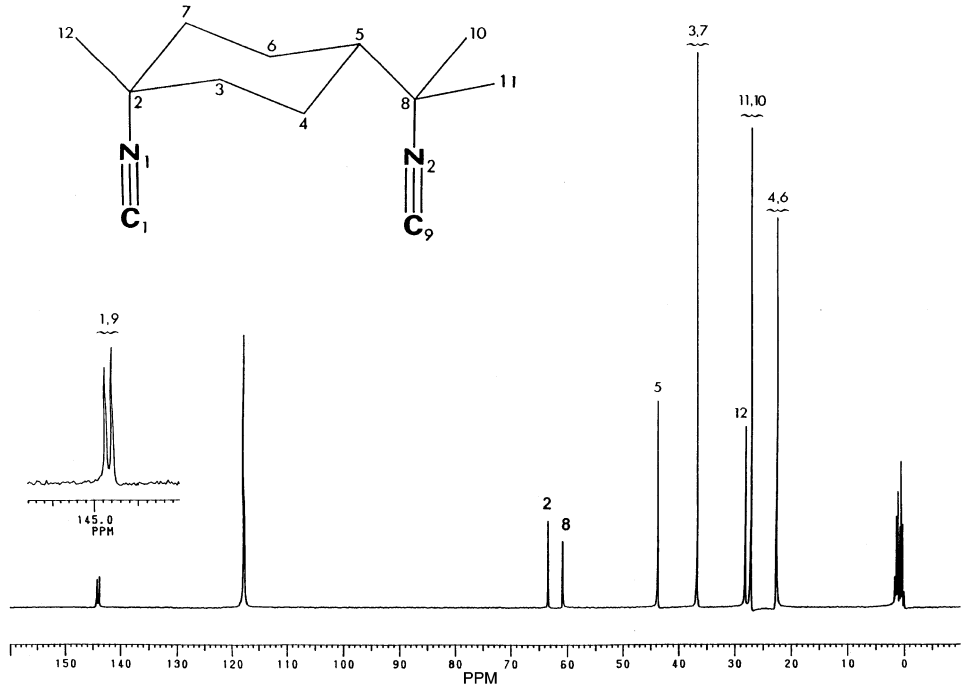

Fig. 18. ^{13}C-NMR spectrum of dmb in acetonitrile-d_3, along with the peak assignments. For the T_1 measurements, peak no. 2 was used.

a function of the M_W or the metals. Bearing in mind the rigid stick nature of the polymer chains, this phase change is clearly not related to chain motion. Rather, evidence for a dependence molecular dimension and material morphology on T_c, were provided [87]. The greater the dimension was, or more amorphous the material was, the greater T_c was.

The $\{[Ag(dmb)_2]TCNQ\}_n$ polymers proved interesting in solutions as they experience reversible structural isomerization from $\{Ag(U\text{-dmb})_2^+\}_n$ to $\{Ag(U\text{-dmb})(Z\text{-dmb})^+\}_n$ to $\{Ag(Z\text{-dmb})_2^+\}_n$ (U- and Z-refer to conformations, Fig. 1) [86]. This isomerization which occurs over a period of several weeks in solutions, is unique only to the $TCNQ^-$ ion. In the solid state, the $TCNQ^-\ldots TCNQ^-$ distance decreases from the U- to the Z-dmb conformation, and an intermediate value is observed for the mixed-conformation polymer, suggesting that these interactions may drive the isomerizations. In addition, benzene and CH_2Cl_2 crystallization molecules are found trapped inside the large loops of the $\{Ag(Z\text{-dmb})_2^+\}_n$ polymers, somewhat helping to retain the structure.

A new family for polymers have been prepared using the $M_4(dmb)_4^{2+}$ unit and bridging ligands (Fig. 20). For instance the crystalline $\{Pd_4(U\text{-dmb})_4(Z\text{-dmb})_2^+\}_n$ polymer have been prepared and crystallographically characterized, and consists of a $(Z\text{-dmb})Pd_4(U\text{-dmb})$ structure. This polymer is issued from the direct reaction between the $Pd_2(dba)_3$, $Pd(O_2CMe)_2$, and dmb [76]. More importantly it is the key

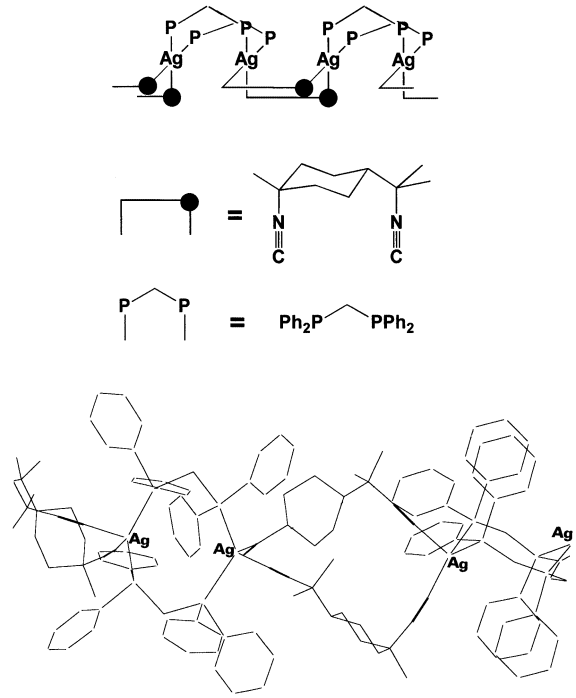

Fig. 19. Segment structure of the mixed-ligand polymer $\{Ag_2(dmb)_2(dppm)_2^{2+}\}_n$.

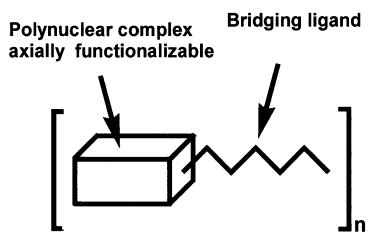

Fig. 20. Scheme showing the general structure of the block-copolymers.

intermediate prior to the addition of PPh_3 during the preparation of the $Pd_4(dmb)_4(PPh_3)_2^{2+}$ cluster. The Pd_4 linear core exhibit Pd–Pd bond lengths of 0.5973(18) (inner), and 2.6080(18) and 2.6080(18) Å (outers), and the expected catenate structure. The polymer exhibits a strong $d\sigma^*$–$d\sigma^*$ absorption at 490 and 488 nm in butyronitrile and ethanol glasses at 77 K, respectively, and are luminescent under the same conditions ($\lambda_{max} = 703$ and 698 nm with FWHM of 2850 and 2800 cm^{-1} and $= 1.00 \pm 0.02$ and 1.14 ± 0.05 μs, respectively [76]). This strategy of making organometallic copolymers has been extended to materials of the type $\{Pt_4(dmb)_4(Ph_2P(CH_2)_mPPh_2)^{2+}\}_n$ ($m = 4$, 5, 6) [77]. The materials are amorphous and no X-ray structure is available. Viscosity measurements indicated that the M_n

varied from 84 000 to 307 000, which correspond to a number of 40 to 150 units. Interestingly, there was a direct relationship between T_1 of the 63 ppm peak (C # 2) and M_n. The $d\sigma^*-d\sigma^*$ bands have been located at 349 nm in all three cases using ethanol as a solvent, and luminescence have been detected in the 736 to 755 nm range with τ_e varying from 4.78 to 5.17 ns. The large energy gap between absorption and emission strongly suggest that these emissions are phosphorescence.

The methodology of linking axially substituted linear polynuclear fragments can be applied to other species such as the $Pd_2(dmb)_2X_2$ dimers (X = Cl, Br) and dppm. The weakly soluble materials analyzed as $Pd_2(dmb)_2(dppm)Cl_2$, and the ^{1}H-NMR data also confirmed the 2:1 dmb/dppm ratio [31]. Unfortunately no single crystal suitable for X-ray analysis was available, but computer modeling (Fig. 21) demonstrates that the polymer chain formulated as $\{[Pd_2(dmb)_2(dppm)]X_2\}_n$ (X = Cl, Br) exhibits limited degrees of freedom, and small cyclic oligomers of this material is very unlikely. The presence of Pd_2 bonding is evidenced by the $d\sigma-d\sigma^*$ signature at 376 nm for both polymers, a band that exhibits the expected significant decrease in FWHM with the lowering of the temperature.

6.3. Properties and applications

The $\{[M(dmb)_2]Y\}_n$ polymers (M = Ag, Cu; $Y = PF_6^-$, BF_4^-, ClO_4^-, NO_3^-) are luminescent in the solid state at room temperature, and at 77 K both in frozen

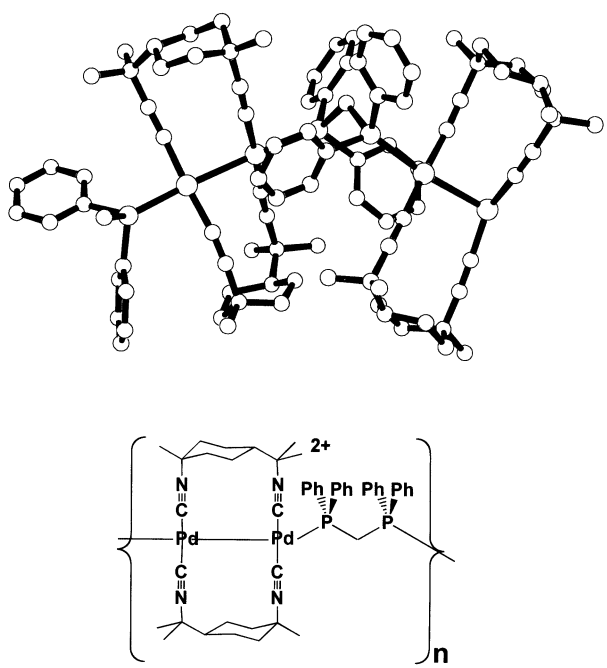

Fig. 21. Computer modeling of the block-copolymer $\{Pd_2dmb)_2(dppm)^{2+}\}_n$.

solutions and in the solid phase [18]. Both series of materials exhibit very broad emissions around 500 nm. However the emission decay curves are poly-exponential and occur in the μs scale. Unexpectedly, the traces can be superimposed for all conditions for a same temperature (in solutions, large crystal, crushed powder, etc.). Time-resolved emission spectroscopy established that the broad emission envelope is composed of an infinite number of emissions. At the early stage of the decay, the λ_{max} is blue shifted, and at a later delay, the λ_{max} is red shifted (i.e. λ_{max} is function of delay time). The key feature is that at the early stage of the decay curve, both λ_{max} and τ_e are practically identical to that of the mononuclear complexes M(CN-*t*-Bu)$_4^+$ (M = Ag, Cu). This important clue along with the superposition of the decay traces for all experimental conditions indicated the presence of an intramolecular exciton process. This phenomenom is well known in organic solids, but not in organometallics. The excited state is an MLCT (M to π*(CNR) as predicted by DFT calculations, and energy transfer occurs at a distance of 5 Å, the Ag…Ag separation. Hence the luminescence arises from an infinite number of species best described as $\{M(CN\text{-}t\text{-}Bu)_4^+\}_n$ where *n* ranges from 1 to theoretically, the end of the polymeric chain.

When the counter-anion Y is replaced by $TCNQ^-$, then the $TCNQ^-$ tends to dimerize [86]. Doping with TCNQ° provides new materials of the type $\{[M(dmb)_2TCNQ.\ xTCNQ°\}_n$ with M = Ag, Cu and $x = 0.5$, 1, and 1.5 [87]. The two latter are semi-conducting as verified from conductivity measurements as a function of temperature. Both polymers $x = 1$ and $x = 1.5$ exhibit similar conductivities, but the more amorphous Cu ones are better resistors. The presence of electric conductivity is indicative of π-stacking of the $TCNQ^{x-}$ species, and the more amorphous the materials, the less ordered is the π-stacking. The $\{[Ag(dmb)_2]TCNQ{\cdot}1.5TCNQ°\}_n$ X-ray structure reveals $\{Ag(dmb)_2^+\}_n$ rods placed parallel forming a multi-cationic layer. Above it, resides a layer of parallel π-stacked $\{TCNQ^{x-}\}_n$ chains. The angle between the $\{Ag(dmb)_2^+\}_n$ and $\{TCNQ^{x-}\}_n$ is about 52°, and the X-ray powder patterns indicate isostructurality with the Cu analogue [87]. For the semi-conducting $\{[M(dmb)_2]TCNQ{\cdot}TCNQ°\}_n$ materials, the similarity suggests similarity in structure with the $x = 1.5$TCNQ° materials. Indeed indexation of the X-ray powder diffraction patterns supports this assumption [87].

One of the most unexpected feature is the presence of photoconductivity for the $\{[Cu(dmb)_2]TCNQ{\cdot}TCNQ°\}_n$ material [87]. Indeed upon visible light irradiation (using a water jacketed filter to avoid sample heating), the conductivity increases reversibly by 20%. Photochemical experiments, photophysical quenching measurements, and comparison with the photo-inert Ag analogue, establish that photo-induced electron transfer from the Cu(I) center to the $\{TCNQ^{x-}\}_n$ chain, occurs to explain the photoconductivity. According to the literature, the photoconductivity for $\{TCNQ^{x-}\}_n$ materials appears unprecedented.

Using this photo-conducting material, photovoltaic cells have been designed. Devices of the type Al/$\{[Cu(dmb)_2]TCNQ{\cdot}TCNQ°\}_n$ as a film/SnO_2 generate electricity at a modest yield. By changing TCNQ° by C_{60}, the quantum yield decreases due to poor π-stacking (flat versus ball geometries). Doping with the better electron acceptor and planar TCNN instead of TCNQ° induces an increase in cell efficiency,

although slightly. The relatively modest performance of the cells has been rationalized, in part, by the slow kinetic for electron transfer from the Cu(I) center, through the insulating alkane section of the dmb ligand, to the semi-conducting $\{TCNQ^{x-}\}_n$ chains.

7. Conclusions

The title diisocyanide compounds are versatile materials, primarily for their ability to assemble metal atoms in so many various ways. Generations of M_2 bonded and non-bonded dimers, cyclic and acyclic trimers, linear and non-linear tetramers, and polymers, with a variety of M_2 separations, have been demonstrated. Some examples of their reducing behavior are known and their MO π*(CNR) contribution in the excited states are seen, and even monitored by time-resolved vibrational spectroscopy, and high resolution electronic spectroscopy. More importantly many of their coordination complexes exhibit interesting properties such as photo-induced H_2 evolution and electro-catalysis, properties that stem directly from the M_2 assembling behavior of these ligands. Recent advances have also been made in the areas of material science, where new organometallic polymers exhibiting properties such as glass transitions, luminescence and intrachain exciton behavior, have been demonstrated. Using the very convenient rigid stick properties of their structures, parallel π-stacking of organic metals has been made to afford new forms of materials, exhibiting semi- and photoconductivity, and even keeping the glass transition behavior. Photovoltaic cells have been designed. The assembling property which appears as an important asset for these ligands, now turns into an inconvenience in these energy conversion cells, as the ligand itself, acts as a resistor.

In comparison with the diphosphines, the chemistry of the diisocyanide ligands appears clearly under developed, as much remain to be explored throughout the transition metal series with the various oxidation states. Molecular shapes, M_2 distances, and nature of the M atoms, are properties that are direct parameters controlling the physical behavior and reactivity. Limitations are found in the relative sensitivity to oxidants, acids (in some occasions), and heat.

8. Codes

b	1,3-diisocyanopropane
4-b	1,4-diisocyanobutane
diiso	diisocyanide ligand
dmb	1,8-diisocyano-*p*-menthane
dppm	bis(diphenylphosphino)methane
MLCT	metal-to-ligand charge transfer
Py	pyridine
tmb	2,5-diisocyano-2′,5′-dimethylhexane
tmi	3,3,6,6-tetramaethylaza-1-cyclohexane-2-ide

Acknowledgements

The Natural Sciences and Engineering Council of Canada (NSERC) and the Fonds Concertés pour l'Avancement de la Recherche (FCAR) for funding allowing research on these ligands in Sherbrooke.

References

[1] H.B. Gray, A.W. Maverick, Science 214 (1981) 1201.
[2] I.S. Sigal, K.R. Mann, H.B. Gray, J. Am. Chem. Soc. 102 (1980) 7252.
[3] V.M. Miskowski, I.S. Sigal, K.R. Mann, H.B. Gray, G.S. Hammond, S.J. Milder, P.R. Ryason, J. Am. Chem. Soc. 101 (1979) 4383.
[4] K.R. Mann, N.S. Lewis, V.M. Miskowski, D.K. Erwin, G.S. Hammond, H.B. Gray, J. Am. Chem. Soc. 99 (1977) 5525.
[5] D.C. Boyd, P.A. Matsch, M.M. Mixa, K.R. Mann, Inorg. Chem. 25 (1986) 3331.
[6] A.G. Sykes, K.R. Mann, J. Am. Chem. Soc. 110 (1988) 8252.
[7] A.G. Sykes, K.R. Mann, J. Am. Chem. Soc. 112 (1990) 7247.
[8] D. Perreault, M. Drouin, A. Michel, P.D. Harvey, Inorg. Chem. 31 (1992) 3688.
[9] P.D. Harvey, D. Fortin, Coord. Chem. Rev. 171 (1998) 351.
[10] J. March, Advanced Organic Chemistry: Reactions, mechanisms, and structures, fourth ed., Wiley, New York, 1992.
[11] W.P. Weber, G.W. Gokel, Tetrehedron Lett. (1972) 1637.
[12] C.-M. Che, W.T. Wong, T.F. Lai, H.L. Kwong, J. Chem. Soc., Chem. Commun. (1989) 243.
[13] C.-M. Che, H.-K. Yip, W.-T. Wong, T.-F. Lai, Inorg. Chim. Acta 197 (1992) 177.
[14] D. Perreault, M. Drouin, A. Michel, P.D. Harvey, Inorg. Chem. 30 (1991) 1.
[15] P.D. Harvey, K.D. Truong, K.T. Aye, M. Drouin, A.D. Bandrauk, Inorg. Chem. 33 (1994) 2347.
[16] D. Perreault, M. Drouin, A. Michel, V.M. Miskowski, W.P. Schaefer, P.D. Harvey, Inorg. Chem. 31 (1992) 695.
[17] H. Xiao, K.-K. Cheung, C.-M. Che, J. Chem. Soc, Dalton Trans. (1996) 3699.
[18] D. Fortin, M. Drouin, M. Turcotte, P.D. Harvey, J. Am. Chem. Soc. 119 (1997) 531.
[19] D. Piché, P.D. Harvey, Can. J. Chem. 72 (1994) 705.
[20] D. Perreault, M. Drouin, A. Michel, P.D. Harvey, Inorg. Chem. 32 (1993) 1903.
[21] D. Fortin, M. Drouin, P.D. Harvey, F.G. Herring, D.A. Summers, R.C. Thompson, Inorg. Chem. 38 (1999) 1253.
[22] F.A. Cotton, G. Wilkinson, P.L. Gauss, Basic Inorganic Chemistry, second ed., Wiley, New York, 1994, p. 61.
[23] C.-M. Che, F.H. Herbsterin, W.P. Schaefer, R.E. Marsh, H.B. Gray, Inorg. Chem. 23 (1984) 2572.
[24] D. Perreault, M. Drouin, A. Michel, P.D. Harvey, Inorg. Chem. 31 (1992) 2740.
[25] W.L. Gladfelter, H.B. Gray, J. Am. Chem. Soc. 102 (1980) 5909.
[26] P.D. Harvey, Z. Murtaza, Inorg. Chem. 32 (1993) 4721.
[27] P.D. Harvey, Coord. Chem. Rev. 153 (1996) 175.
[28] Y. Yamamoto, H. Yamazaki, Inorg. Chem. 25 (1986) 3327.
[29] R. Provencher, P.D. Harvey, Inorg. Chem. 35 (1996) 2113.
[30] G. Nembra, P. Lemoine, P. Braunstein, C.D. Debellefon, M. Ries, J. Organomet. Chem. 304 (1986) 245.
[31] N. Jourdan, M. Sc. Dissertation, Université de Sherbrooke, 1992.
[32] W.L. Gladfelter, H.B. Gray, J. Am. Chem. Soc. 102 (1980) 5909.
[33] K.R. Mann, N.S. Lewis, R.M. Williams, H.B. Gray, J.G. Gordon II, Inorg. Chem. 17 (1978) 828.
[34] K.R. Mann, J.G. Gordon II, H.B. Gray, J. Am. Chem. Soc. 97 (1975) 3553.
[35] N.S. Lewis, K.R. Mann, J.G. Gordon II, H.B. Gray, J. Am. Chem. Soc. 98 (1976) 7461.

[36] V.M. Miskowski, G.L. Nobinger, D.S. Kliger, G.S. Hammond, N.S. Lewis, K.R. Mann, H.B. Gray, J. Am. Chem. Soc. 100 (1978) 485.
[37] R.F. Dallinger, V.M. Miskowski, H.B. Gray, W.H. Woodruff, J. Am. Chem. Soc. 103 (1981) 1595.
[38] K.R. Mann, J.A. Thich, R.A. Bell, C.L. Coyle, H.B. Gray, Inorg. Chem. 19 (1980) 2462.
[39] K.R. Mann, H.B. Gray, Adv. Chem. Ser. 173 (1979) 225.
[40] K.R. Mann, Cryst. Struct. Commun. 20 (1981) 1921.
[41] C.L. Extrom, D. Britton, K.R. Mann, M.G. Hill, V.M. Miskowski, W.P. Schaefer, H.B. Gray, W.M. Lamanna, Inorg. Chem. 35 (1996) 549.
[42] D.C. Smith, R.E. Marsh, W.P. Schaefer, T.M. Loehr, H.B. Gray, Inorg. Chem. 19 (1990) 534.
[43] V.M. Miskowski, S.F. Rice, H.B. Gray, R.F Dallinger, S.J. Milder, M.G. Hill, C.L. Extrom, K.R. Mann, Inorg. Chem. 33 (1994) 2799.
[44] D.C. Smith, Ph.D. Dissertation, California Institute of Technology, 1989.
[45] D.C. Smith, V.M. Miskowski, W.R. Mason, H.B. Gray, J. Am. Chem. Soc. 112 (1990) 3759.
[46] S.F. Rice, H.B. Gray, J. Am. Chem. Soc. 103 (1981) 1593.
[47] S.K. Doorn, K.C. Gordon, R.B. Dyer, W.H. Woodruff, Inorg. Chem. 31 (1992) 2284.
[48] S.J. Milder, R.A. Goldbeck, D.S. Kliger, H.B. Gray, J. Am. Chem. Soc. 102 (1980) 6761.
[49] S.F. Rice, S.J. Milder, H.B. Gray, R.A. Goldbeck, D.S. Kliger, Coord. Chem. Rev. 43 (1982) 349.
[50] J.R. Winkler, J.L. Marshall, T.L. Netzel, H.B. Gray, J. Am. Chem. Soc. 108 (1986) 2262.
[51] A.G. Sykes, Ph.D. Dissertation, University of Minnesota, 1988.
[52] S.F. Rice, Ph.D. Dissertation, California Institute of Technology, 1982.
[53] S.J. Milder, D.S. Kliger, L.G. Butler, H.B. Gray, J. Phys. Chem. 90 (1986) 5567.
[54] D.C. Smith, H.B. Gray, Coord. Chem. Rev. 100 (1990) 169.
[55] M.G. Hill, A.G. Sykes, K.R. Mann, Inorg. Chem. 32 (1993) 783.
[56] S.C. Cheng, C.A. Blaine, M.G. Hill, K.M. Mann, Inorg. Chem. 35 (1996) 7704.
[57] M.R. Rhodes, K.R. Mann, Inorg. Chem. 23 (1984) 2053.
[58] J.S. Najdzionek, B.D. Santarsiero, Acta Crystallogr. Sect. C 39 (1983) 577.
[59] M.M. Mixa, Ph.D Dissertation, University of Minnesota, 1986.
[60] M.G. Hill, K.R. Mann, Inorg. Chim. Acta 243 (1996) 219.
[61] D. Fortin, Ph.D. Dissertation, Université de Sherbrooke, 1998.
[62] V.M. Miskowski, T.P. Smith, T.M. Loehr, H.B. Gray, J. Am. Chem. Soc. 107 (1985) 7925.
[63] M.M. Olmstead, A.L. Balch, J. Organomet. Chem. 148 (1978) C15.
[64] A.W. Maverick, T.P. Smith, E.F. Maverick, H.B. Gray, Inorg. Chem. 26 (1987) 4336.
[65] A.L. Balch, J.R. Boehm, H. Hope, M.M. Olmstead, J. Am. Chem. Soc. 98 (1976) 7431.
[66] R.J.H. Clark, C. Sourisseau, Nouv. J. Chim. 4 (1980) 287.
[67] A.G. Sykes, K.R. Mann, Inorg. Chem. 29 (1990) 4449.
[68] P.D. Harvey, M. Drouin, A. Michel, D. Perreault, J. Chem. Soc., Dalton Trans. (1993) 1365.
[69] H.B. Gray, K.R. Mann, N.S. Lewis, J.A. Thich, R.M. Richman, Adv. Chem. Ser. 168 (1978) 44.
[70] P.K. Eidena, A.W. Maverick, H.B. Gray, Inorg. Chim. Acta 50 (1981) 59.
[71] K.R. Mann, M.J. DiPierro, T.G. Gill, J. Am. Chem. Soc. 102 (1980) 3964.
[72] V.M. Miskowski, H.B. Gray, Inorg. Chem. 26 (1987) 1108.
[73] K.R. Mann, B.A. Parkinson, Inorg. Chem. 20 (1981) 1921.
[74] I.S. Sigal, H.B. Gray, J. Am. Chem. Soc. 103 (1981) 2220.
[75] H.B. Gray, V.M. Miskowski, S.J. Milder, T.P. Smith, A.W. Maverick, J.D. Buhr, W.L. Gladfelter, I.S. Sigal, K.R. Mann, in: M. Tsutsui (Ed.), Fundamental Research in Homogeneous Catalysis 3, Plenum Press, New York, 1979, pp. 819–834.
[76] T. Zhang, M. Drouin, P.D. Harvey, Inorg. Chem. 38 (1999) 1305.
[77] T. Zhang, M. Drouin, P.D. Harvey, Inorg. Chem. 38 (1999) 957.
[78] M.M. Mixa, A Sykes, K.R. Mann, Inorg. Chem. Acta 160 (1989) 159.
[79] D.A. Bohling, T.P. Gill, K.R. Mann, Inorg. Chem. 20 (1981) 194.
[80] L.F. Dahl, R.E. Rundle, Acta Crystallogr. 16 (1963) 419.
[81] M.G. Hill, J.P. Bullock, T. Wilson, P. Bacon, C.A. Blaine, K.R. Mann, Inorg. Chim. Acta 226 (1994) 61.

[82] W.L. Gladfelter, M.W. Lynch, W.P. Schaefer, D.N. Hendrickson, H.B. Gray, Inorg. Chem. 20 (1981) 2390.
[83] T. Zhang, M. Drouin, P.D. Harvey, Inorg. Chem. 38 (1999) 4928.
[84] A. Guitard, A. Mari, A.L. Beauchamp, Y. Dartiguenave, M. Dartiguenave, Inorg. Chem. 22 (1983) 1603.
[85] M. Dartiguenave, Y. Dartiguenave, A. Mari, A. Guitard, M.J. Olivier, A.L. Beauchamp, Can. J. Chem. 66 (1988) 2386.
[86] D. Fortin, M. Drouin, P.D. Harvey, J. Am. Chem. Soc. 120 (1998) 5351.
[87] D. Fortin, M. Drouin, P.D. Harvey, Inorg. Chem. 39 (2000) 2758.
[88] F. Lebrun, M.Sc. Dissertation, Université de Sherbrooke, 2001.